

University of Alberta

Failure Analysis of Downhole Valves Using Finite Element Methods

by

Christopher J. Hutton



A thesis submitted to the Faculty of Graduate Studies and Research in partial fulfillment of the requirements for the degree of Master of Science.

Department of Mechanical Engineering

Edmonton, Alberta
Fall 1996



National Library
of Canada

Acquisitions and
Bibliographic Services Branch

395 Wellington Street
Ottawa, Ontario
K1A 0N4

Bibliothèque nationale
du Canada

Direction des acquisitions et
des services bibliographiques

395, rue Wellington
Ottawa (Ontario)
K1A 0N4

Your file *Voire référence*

Our file *Notre référence*

The author has granted an irrevocable non-exclusive licence allowing the National Library of Canada to reproduce, loan, distribute or sell copies of his/her thesis by any means and in any form or format, making this thesis available to interested persons.

L'auteur a accordé une licence irrévocable et non exclusive permettant à la Bibliothèque nationale du Canada de reproduire, prêter, distribuer ou vendre des copies de sa thèse de quelque manière et sous quelque forme que ce soit pour mettre des exemplaires de cette thèse à la disposition des personnes intéressées.

The author retains ownership of the copyright in his/her thesis. Neither the thesis nor substantial extracts from it may be printed or otherwise reproduced without his/her permission.

L'auteur conserve la propriété du droit d'auteur qui protège sa thèse. Ni la thèse ni des extraits substantiels de celle-ci ne doivent être imprimés ou autrement reproduits sans son autorisation.

ISBN 0-612-18274-6

Canada



Petrovalve International Inc.

209-8915 51st Avenue, Edmonton, Alberta Canada T6E 5J3
Telephone: (403) 468-1159 • Fax: (403) 468-1164 • Trading Symbol: FTK

May 7, 1996

4-9 Mechanical Engineering
University of Alberta
Edmonton T6G 2G8
Fax: 492-2200

Attn: Chris Hutton
Re: Permission to Use Graphics

Chris:

The purpose of this letter is to grant you permission to use graphics from the Petrovalve product brochures for use in your Thesis report.

Best Regards,

Greg Ogaranko

University of Alberta

Library Release Form

Name of Author: Christopher J. Hutton


Title of Thesis: Failure Analysis of Downhole Valves Using Finite Element Methods

Degree: Master of Science

Year this Degree Granted: 1996

Permission is hereby granted to the University of Alberta Library to reproduce single copies of this thesis and to lend or sell such copies for private, scholarly or scientific research purposes only.

The author reserves all other publication and other rights in association with the copyright in the thesis, and except as hereinbefore provided, neither the thesis nor any substantial portion thereof may be printed or otherwise reproduced in any material form whatever without the author's prior written permission.

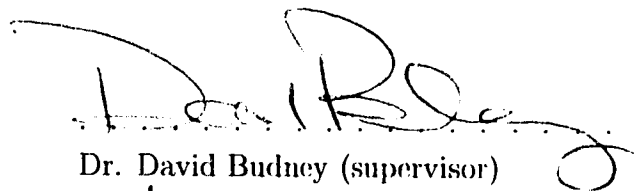

.....
Christopher J. Hutton
73 Fairway Drive
Edmonton, Alberta
Canada, T6J 2C2

Date: *August 28/96*

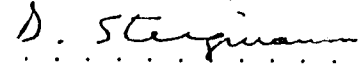
University of Alberta

Faculty of Graduate Studies and Research

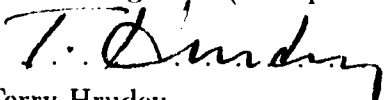
The undersigned certify that they have read, and recommend to the Faculty of Graduate Studies and Research for acceptance, a thesis entitled **Failure Analysis of Downhole Valves Using Finite Element Methods** submitted by Christopher J. Hutton in partial fulfillment of the requirements for the degree of Master of Science.



Dr. David Budney (supervisor)




Dr. David Steigmann (co-supervisor)



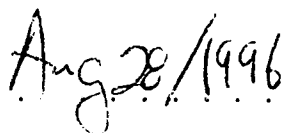
Dr. Terry Hruday



Dr. Roger Toogood



Dr. M. Gary Faulkner

Date: 

To my Dad who gave me my love for engineering.
Thank you for your guidance and support.

Abstract

The design of downhole valves used in pump jacks to recover oil from underground oil wells has remained constant for decades. Recently, an alternative valve design has been developed which greatly increases the oil production from these wells. While the performance of the valves from a fluid dynamics perspective is excellent, the structural performance is somewhat poorer than that of the industry standard valves.

For this thesis, research was done using finite element methods in an effort to understand the failure mechanics of this new valve design. Understanding why the failures occur made it possible to improve the structural strength of the valves without compromising the fluid dynamics performance.

Acknowledgements

There are several people who deserve mention for helping me complete my work on this project.

Flotek Industries, the parent company to Petrovalve International, sponsored this research. Their technology was the basis for this research project. I would like to thank Larry Shaben, Doug Jensen, George Kirkwood, and Greg Ogaranko for their insight and industry knowledge throughout this project.

My thesis advisor, Dr. Dave Budney was always a great resource and friend. My co-advisor Dr. David Steigmann was also a great source for information and encouragement.

My best friend Jenna, who is now my wife, was always there to listen and support me through the high and low times. She was always there to steer me back toward finishing my project whenever I strayed away. My family provided me with a tremendous amount of support and encouragement. All my friends in the department, including Stef, Steve, Matt, Jeff, Rob, Dave, and John, among many others, were there to bounce ideas off of and to relax and take a break with.

I would also like to thank Mark Ackerman for keeping the computer system up and running even though I tried my hardest to bring it down on a regular basis.

Contents

| | | |
|----------|--|-----------|
| 1 | Introduction | 1 |
| 2 | Failure Prediction | 9 |
| 2.1 | Loading Conditions | 9 |
| 2.1.1 | Preload | 9 |
| 2.1.2 | Fluid Pressure Loading | 11 |
| 2.1.3 | Lab Simulation | 12 |
| 2.2 | Failure Criteria | 13 |
| 2.2.1 | Material Properties | 14 |
| 2.2.2 | Failure Criteria in Ansys | 15 |
| 2.2.3 | Coulomb-Mohr Failure Criterion | 16 |
| 2.3 | Observed Failures | 19 |
| 2.3.1 | Field Failures | 20 |
| 2.3.2 | Lab Failures | 21 |
| 3 | Frictionless Contact Modeling | 24 |
| 3.1 | Finite Element Meshing | 24 |
| 3.1.1 | Element Selection and Mesh Density | 24 |
| 3.1.2 | Contact Elements | 27 |
| 3.2 | Initial Guided Stem Design | 27 |
| 3.3 | Modifications to the Seat Design | 32 |
| 3.3.1 | Undercut Shoulder | 33 |

| | | |
|----------|---|-----------|
| 3.3.2 | Lowered Contact Point | 35 |
| 3.3.3 | Increased Contact Angle | 38 |
| 4 | Lab Testing | 41 |
| 4.1 | Destructive Testing | 41 |
| 4.1.1 | Test Setup | 42 |
| 4.1.2 | Test Results | 44 |
| 4.2 | Strain Gauge Study | 47 |
| 4.2.1 | Test Setup | 47 |
| 4.2.2 | Test Results | 48 |
| 5 | Frictional Contact Modeling | 55 |
| 5.1 | Influence of Contact Parameters | 55 |
| 5.1.1 | Determining Contact Stiffness and Sliding Stiffness | 56 |
| 5.1.2 | Sensitivity to Small Changes in Young's Modulus and Poisson's Ratio | 58 |
| 5.1.3 | Symmetric Meshing | 59 |
| 5.1.4 | Location of Strain Measurement | 61 |
| 5.2 | Determining the Frictional Coefficients | 63 |
| 5.3 | Failure Predictions | 65 |
| 6 | Conclusions and Future Work | 69 |
| | Bibliography | 72 |

List of Figures

| | | |
|-----|---|----|
| 1.1 | Picture of API Design Downhole Valve | 2 |
| 1.2 | Fluid Movement Over Two Pumping Cycles | 3 |
| 1.3 | API vs. New Valve Design | 4 |
| 1.4 | Guided Stem Design | 5 |
| 1.5 | Example of Three Valve Sizes | 6 |
| 2.1 | Traveling Valve Assembly Diagram | 10 |
| 2.2 | Ball With Stem Removed | 13 |
| 2.3 | Coulomb-Mohr Failure Criterion - σ vs. τ | 17 |
| 2.4 | Coulomb-Mohr Failure Criterion - σ_1 vs. σ_3 | 18 |
| 2.5 | Three Valves Broken In Service | 21 |
| 2.6 | Cracked Valve Shown With Dye Penetrant | 22 |
| 2.7 | Lab Failure of a Cast Cobalt Valve | 23 |
| 2.8 | Lab Failure of a Nickel Carbide Valve | 23 |
| 3.1 | Finite Element Mesh for a 2" Nickel Carbide Valve | 25 |
| 3.2 | Effects of Changes in Mesh Density on a 2" Nickel Carbide Valve | 26 |
| 3.3 | Loading Due to Hydrostatic Pressure | 29 |
| 3.4 | Loading Due to the Preload | 29 |
| 3.5 | VonMises Distribution, 2" Nickel Carb. Original Design | 30 |
| 3.6 | Coulomb-Mohr Ratio, 2" Nickel Carb. Original Design | 30 |
| 3.7 | Coulomb-Mohr Ratio Including the Preload | 31 |
| 3.8 | Closeup of Stress Concentration using VonMises Criterion | 32 |

| | | |
|------|--|----|
| 3.9 | VonMises Distribution Showing Undercut to Shoulder Region | 33 |
| 3.10 | Coulomb-Mohr Ratio Showing Undercut to Shoulder Region | 34 |
| 3.11 | Quarter Section Drawing Showing Lowered Point of Contact | 35 |
| 3.12 | Lowered Contact Point - VonMises Distribution | 36 |
| 3.13 | Lowered Contact Point - Coulomb Mohr Ratio | 36 |
| 3.14 | Coulomb Mohr Ratio Showing Reduced Lip Height | 37 |
| 3.15 | Effect of Contact Angle on Reaction Force | 38 |
| 3.16 | Coulomb-Mohr Ratio of Final Modified Design | 40 |
| 4.1 | Picture of Compression Test Setup | 43 |
| 4.2 | Close Up Picture of Valve In Compression Test | 44 |
| 4.3 | Load Strain Curve - Oil Lubrication | 48 |
| 4.4 | Reloading After Partial Unloading | 49 |
| 4.5 | Unload to Before the Change in Slope and Reload | 51 |
| 4.6 | Normal and Frictional Load On Seat When Loading | 52 |
| 4.7 | Normal and Frictional Load On Seat When Unloading | 52 |
| 4.8 | Load Strain Curve - Powdered Graphite Lubrication | 53 |
| 5.1 | Drawing of a Point to Surface Contact Element | 60 |
| 5.2 | Drawing Showing When a Contact Element is Considered | 60 |
| 5.3 | Hoop Strain Distribution - Whole Valve | 62 |
| 5.4 | Hoop Strain Distribution - Breakaway of Lip Region | 63 |
| 5.5 | Reaction to Changing the Coefficient of Friction | 64 |
| 5.6 | Comparing Test Data to Curve Using a Frictional Coefficient of 0.145 | 65 |

List of Tables

| | | |
|-----|--|----|
| 2.1 | Material Properties | 14 |
| 2.2 | Coulomb-Mohr Failure Criteria | 49 |
| 3.1 | Modifications to Contact Angle and Height of Contact Point | 39 |
| 4.1 | Frictionless Predictions and Actual Loads at Failure | 45 |
| 5.1 | Effect of Young's Modulus on Results | 58 |
| 5.2 | Effect of Poisson's Ratio on Results | 59 |
| 5.3 | Frictional Versus Frictionless Failure Load Predictions | 66 |

Chapter 1

Introduction

This thesis is a study of downhole valve technology. It focuses on determining the failure mechanisms of a new valve design and from this, find modifications that can be made to the design to improve the structural strength of the valves.

According to industry statistics [6] there are approximately 920 000 oil wells scattered around the world producing about 60 000 000 barrels of oil per day. Roughly 90% of these wells are pumping wells, of which approximately 95% use pump jacks to recover the oil. The pump jack is essentially the driver for a positive displacement pump. It rocks up and down, alternately pushing and pulling a pump rod into and out of the ground. The pump rod travels inside a stationary casing that extends the entire depth of the well, often hundreds of meters below the surface. At the bottom of the well are a pair of valves. One, called the traveling valve, is attached to the pump rod. The other, called the standing valve, is fixed to the casing. These valves typically consist of a hollow cylindrical seat with a beveled inside top corner that mates with a spherical ball. A photograph of this type of valve can be seen in Figure 1.1. The two valves work as a pair, one stationary, and one moving up and down with the pump rod. Their job is to allow fluid to pass only in one direction (ie. up to the surface of the well). When fluid pressure is higher below the valve than above, the ball is lifted off of the seat and the oil passes through the valve. When the fluid pressure is higher above the valve, the ball is pressed into the seat, sealing the valve and preventing any flow

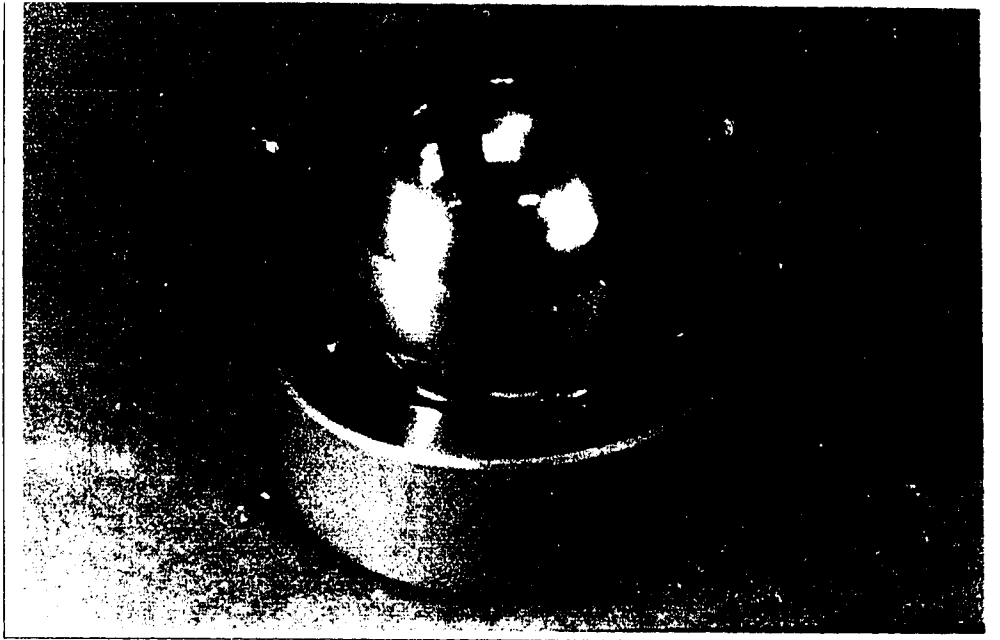


Figure 1.1: Picture of API Design Downhole Valve

from passing backward through the valve. The traveling valve closes when the pump rod ascends, lifting fluid to the surface. It opens and allows fluid to pass through when the pump rod descends. The standing valve, which is below the traveling valve, opens when the pump rod ascends, allowing fluid to be drawn into the region between the two valves. It closes when the pump rod descends to prevent any fluid from returning to the reservoir below. This alternate opening and closing of the two valves allows the fluid to be pumped to the surface. Figure 1.2 demonstrates the movement of fluid through the valves over two pumping cycles.

The valves studied for this thesis have been modified from the API standard design to provide improved fluid dynamics performance and reduced wear. A drawing showing both the API valve and the new design can be seen in Figure 1.3 [7]. The numbers shown in the figure coincide with the different parts of the valve listed below. The spherical ball^[1] used in the API valve shown on the left of the figure is replaced, in the new design, by a hemisphere^[2] with a stem mounted through its center axis, extending between 25mm and 40mm (depending on the size of the valve) out either side. The seat is also modified. A web^[3] extends across the lower part of the seat and acts as

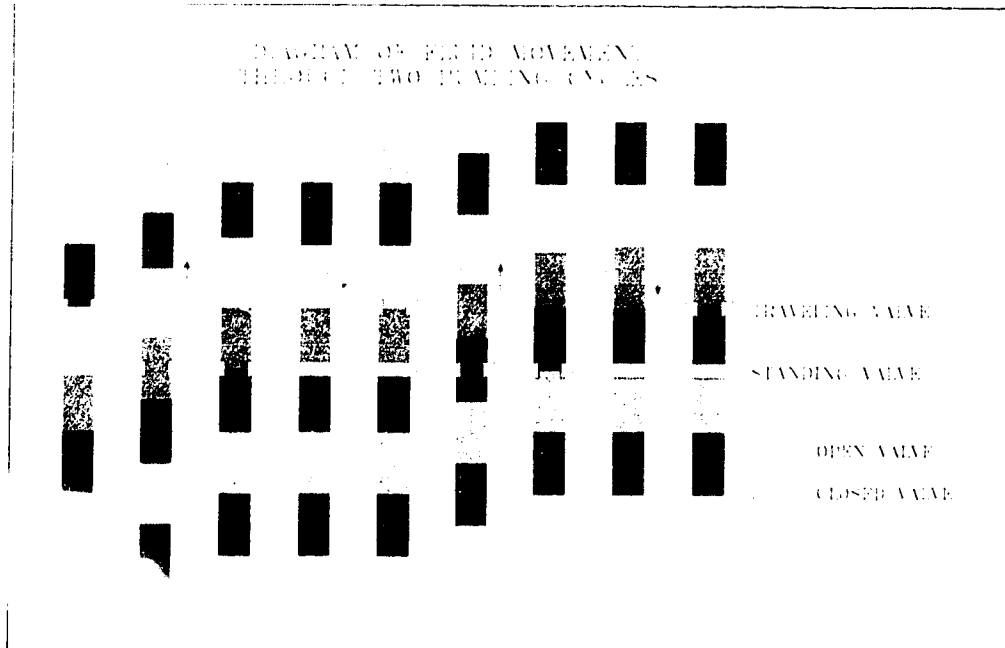


Figure 1.2: Fluid Movement Over Two Pumping Cycles

a guide for the stem on the underside of the ball. Figure 1.4 [7] is a picture of the guided stem design with the web clearly visible across the bottom of the valve. A lip^[4] has been added to raise the contacting surface preventing the ball from making contact with the web. This avoids compromising the sealing capacity of the valve. Unfortunately, this lip region had to be made thinner than the rest of the seat so that the valve would fit into standard API housings (which is necessary for the product to be marketable). On the outside of the seat, at the base of the lip, is a shoulder^[5]. This shoulder is at the same height as the top edge of the standard API valve shown on the left of the Figure 1.3. It seals, upon assembly, against a ledge that is part of the valve housing. The inside surface of the seat is tapered to achieve an increase in flow area (The taper in the valve size shown in Figure 1.3 is relatively small). A smaller diameter at the point of contact with the ball is necessary due to the smaller diameter of the ball itself. A cage^[6] above the valve arrangement has a guide for the upper stem. Figure 1.5 [7] shows the ball, seat, and cage for three different sizes of valve. In the actual assembly the seat and cage are separated by the ledge in the housing.

The ball and the seat are made of the same material which may be tungsten

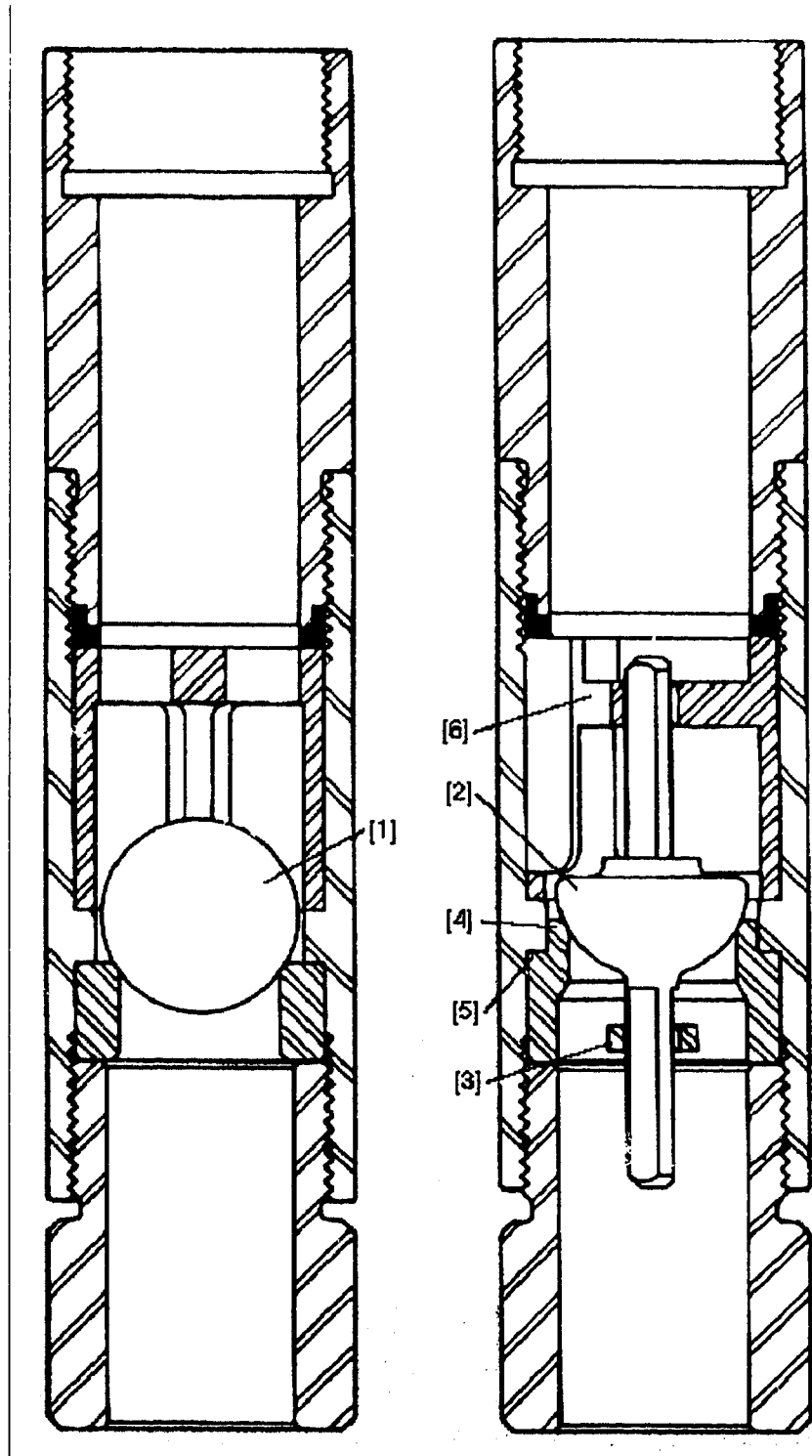
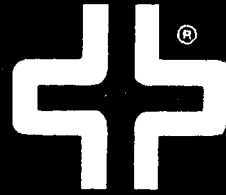


Figure 1.3: API vs. New Valve Design

Petrovalve Plus



The system of artificial lift
that pumps more . . . and lasts longer
with no incremental capital cost

Figure 1.4: Guided Stem Design

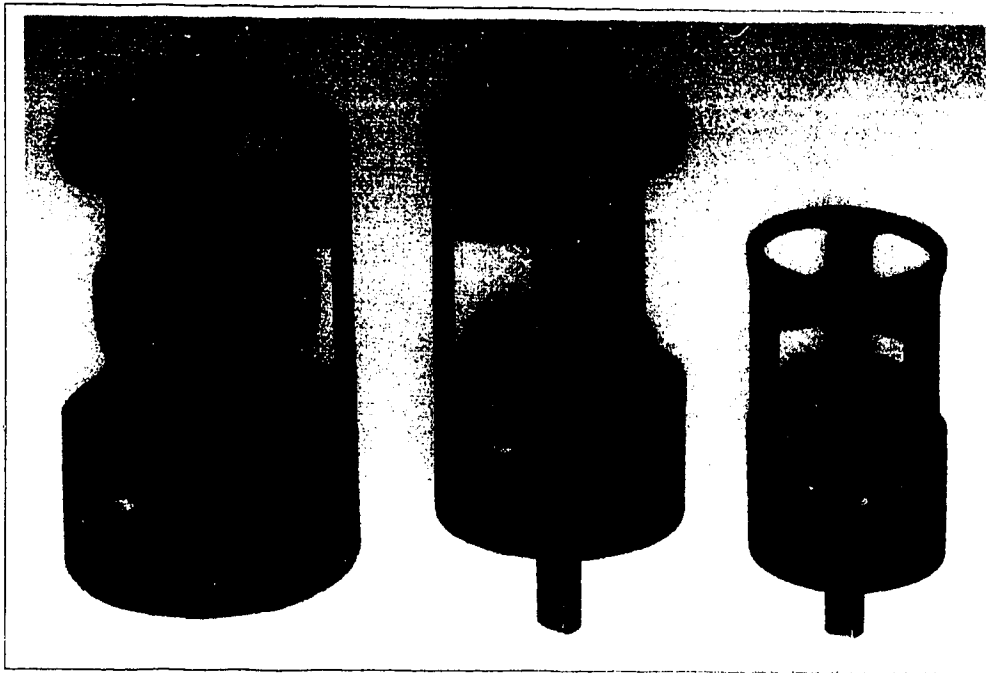


Figure 1.5: Example of Three Valve Sizes

carbide, nickel carbide, or cast cobalt. These materials are very high strength, brittle alloys made with powder metallurgy processes. The manufacturers of the valves could provide only limited information regarding material properties. The accuracy of these values is unknown. It was also necessary to assume values for some of the material properties based on experimental results and observations from this study.

In the guided stem valve arrangement, the ball (hemisphere) is not free to oscillate in the flow, thus preventing marring of the ball's polished surface against the valve housing. In API standard valves the marring is sometimes reduced by using a larger ball to lower the magnitude of oscillation. This results in less space between the ball and the wall of the housing so smaller oscillations occur which in turn decreases the magnitude of the impacts when the ball does strike the wall. It follows then, that there is also reduced flow area, increasing flow losses. The hemisphere used in the guided stem design is typically smaller in diameter than the sphere used in the standard API valves. This increases the effective flow area and reduces the flow losses substantially, thus, increasing the efficiency of the pump. The decrease in wear also

allows an effective sealing surface to be maintained over a longer duration of use. The result of this is less 'down-time' for the replacement of worn valves, again, increasing the overall efficiency of the pump. Because of the guides, the ball does not have to 'seek out' the mating surface when the flow reverses but is instead placed directly on it. The time required for the ball to fully seat when the flow begins to reverse is, therefore, substantially reduced compared with the API design. This results in less fluid 'slipping' backward through the valve. Removal of the oscillation also results in fewer disturbances to the flow with lower hydraulic losses. According to studies performed by the valve's developers, simply by changing to this valve arrangement, several wells in Alberta and Saskatchewan have seen increases in flow capacity ranging from 43% to 112% depending on the valve size and the viscosity of the fluid being pumped [7].

These benefits do come at a cost. To maintain a large flow area, the inside diameter of the seat is relatively large. This, coupled with a smaller radius ball results in a contact angle ranging between 17° and 25° to the vertical depending on the size of valve. This compares with contact angles in the range of 45° on standard API valves. These steep angles cause very large radial forces on the seat, as discussed in Section 3.3.3 and as seen in Figure 3.15, leading to large hoop stresses. The thickness of the material is much less in the lip region than in the rest of the valve, further contributing to higher stress levels and reduced overall strength of the valve design. One of the major goals of this study was to reduce these stresses while maintaining the fluid dynamics advantages and the general design concept of the valve.

This thesis investigates the failure mechanisms of the guided stem design as well as studying modifications to this valve design to improve its structural performance without changing the general design or compromising the hydraulic performance. The analysis includes finite element modeling, destructive testing, and strain gauge studies of the valves. Although the materials used are assumed to behave as linear elastic, the solution of the problem is non-linear. This is because of the use of contact elements. The finite element models are two dimensional axisymmetric models with point to

surface contact elements between the bodies. Because the properties of the materials used in the valves are not all available or are considered uncertain it is necessary to determine their values by other means. A discussion of the assumptions made regarding material properties, among other modeling parameters, can be found in Chapter 5. There is a large cost associated with manufacturing test coupons using powder metallurgy processes. The budget for this study did not include an allowance for any lab testing and so standard material property tests are, unfortunately, not viable options for determining these properties directly. The inferred values that are presented are the best estimates possible under the conditions available for this research project. Some additional funding was provided after the initiation of the study to perform a limited number of strain gauge studies and destructive tests.

All finite element work was done using the commercial program Ansys. Unless specifically stated, all data presented in this thesis is for the two inch valve size in the nickel carbide material. Due to the geometric similarities between the different sizes, the trends and findings can be applied to all sizes. Only summary data is presented for the other sizes and materials. For the valves in each material and size a set load is maintained for all the models. This allows for direct comparisons to be made regarding the effectiveness of the various design changes between all of the models presented. The value chosen for this load is that at which failure is predicted for the unmodified guided stem design.

Chapter 2

Failure Prediction

2.1 Loading Conditions

Two loading conditions are imposed on the valve in service; the preload and the fluid pressure. The preload occurs during assembly and the fluid pressure is a cyclic load that is applied and removed on every pump stroke.

2.1.1 Preload

Figure 2.1 is an assembly drawing showing how the valve components are fitted into the traveling valve housing (barrel). The housing for the standing valve is very similar. The preload is imposed on the seat when the components are assembled into the housing. The cage, ball, and seat are all placed in the barrel and screwed components (subs) are used to tighten them into place. Inside the barrel is a ledge which the cage contacts from above and the seat meets from below. The cage is inserted into the top of the barrel and is followed by the top sub. The top sub is tightened down, holding the cage in place against the ledge. The top end of the top sub is used to connect the barrel to the pump rod. The ball and the seat are inserted into the barrel from below such that the shoulder of the seat meets with the bottom of the ledge inside the barrel. The bottom sub or nose is inserted and tightened, imposing a compressive preload on the seat between the base and the shoulder. According to Table 8.1 of

PETROVALVE PLUS VALVE ASSEMBLY

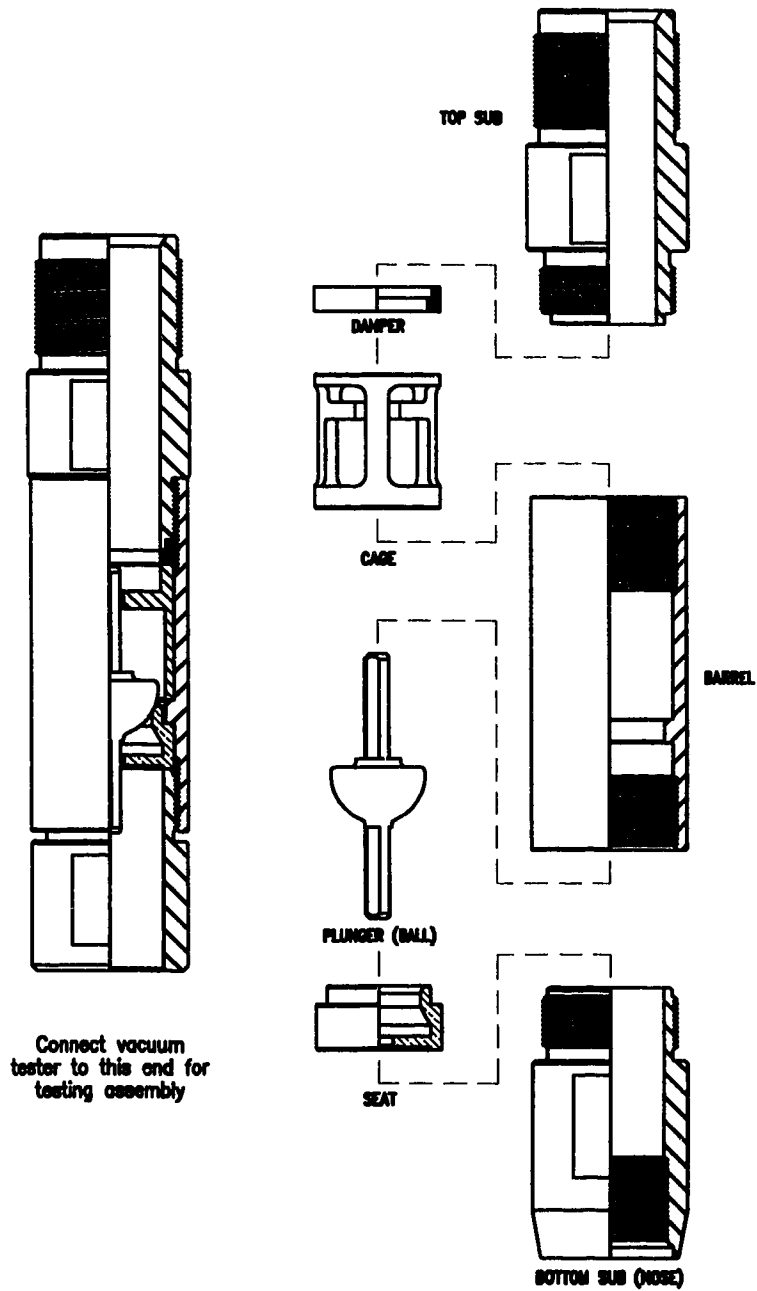


Figure 2.1: Traveling Valve Assembly Diagram

API standard RP 11AR [5], the torque used to tighten the bottom sub into the barrel should range between 150 N·m and 480 N·m for valve sizes $1\frac{1}{4}$ " to $2\frac{1}{4}$ " respectively. Using equations for bolt loading from standard machine component design texts [8], these loads result in a compressive preload ranging from 251 MPa down to 9.2 MPa, again for valve sizes $1\frac{1}{4}$ " to $2\frac{1}{4}$ " respectively. Valve shops assembling the components often severely over tighten the subs. Section 3.2 shows how increasing the preload to over 1000 MPa has a negligible effect on the final failure prediction. Although failures of the valves have been observed while tightening the subs it is likely that this is caused by misalignment of the valves in the housing rather than by the over tightening itself.

2.1.2 Fluid Pressure Loading

The fluid pressure is a function of the depth of the well (static pressure) and of the accelerations imposed by the pump jack (dynamic pressure). The static pressure can be given by the equation:

$$P_{st} = \rho gh \quad (2.1)$$

where ' ρ ' is the density, ' g ' is the acceleration due to gravity, and ' h ' is the depth of the well. The displacement of the pump jack is a sinusoidal function with amplitude of half the stroke length and a frequency equal to the pumping frequency. The acceleration can be found by simply differentiating twice. The dynamic pressure can then be given by the equation:

$$P_{dyn} = \rho ah \quad (2.2)$$

where ' a ' is this acceleration. Summing the static and dynamic components gives:

$$P_{tot} = P_{st} + P_{dyn} = \rho(g + a)h \quad (2.3)$$

This equation represents the maximum working pressure that the traveling valve will see in service when ' a ' is a maximum (ie. at the bottom of the pumping stroke). It should be noted that the pressure exerted on the traveling valve and the standing valve differs. As the pump rod descends, the standing valve is closed and, therefore, experiences the static pressure of the column of oil. When the pump rod begins to

ascend again, the standing valve opens, experiencing no loading. The loading curve is, then, approximated by a square wave which alternates between zero load and the static pressure. As the pump rod descends, the traveling valve is in the open position and experiences no loading. At the bottom of the stroke as the pump rod begins to ascend, the traveling valve experiences its peak loading which is the sum of the static and dynamic loads. This load decreases sinusoidally due to the acceleration term in the above equation for P_{tot} until the pump rod reaches the top of its stroke. At this point the load drops to zero as the valve opens again. The load curve for the traveling valve is, then, a square wave, representing the static load, summed with half of a sine wave, representing the dynamic load. The load curve is zero during what would be the other half of the sine wave (ie. while the valve is open). For large pump jacks working at a high pumping frequency (eg. 7.5m stroke length at 12 strokes per minute) the acceleration can be as high as $\frac{2}{3}g$. For a well with a depth of 3600m this translates into a peak pressure for the traveling valve of nearly 50MPa.

2.1.3 Lab Simulation

Destructive tests were performed on the valve by applying a simulated pressure load with an Instron universal testing machine. The stems were removed from the balls of several different sized valves, as in Figure 2.2, to provide a surface for the test apparatus to apply a load. The valves were placed into the testing machine between steel plates and the cross head applied a vertical compressive load through the plates into the ball and seat. Load application was controlled by displacement for this particular test apparatus. The cross head was lowered at a rate of 0.127mm/minute. Failure usually occurred between 10 and 15 minutes after the loading was initiated. The displacements occurring within the seats were very small. The models predict movement on the order of 0.15mm between the ball and the seat. The rest of the observed displacement is likely the result of the deflection of the cross head and the load cell on the Instron.

This test did not include the effects of the fluid pressure on the exposed surfaces

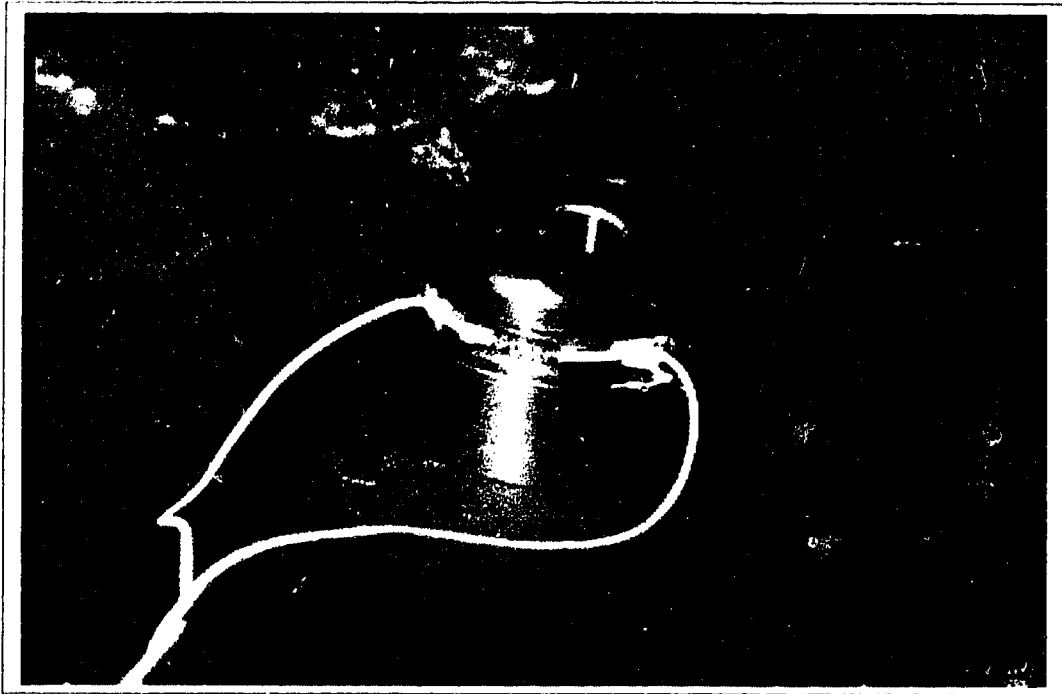


Figure 2.2: Ball With Stem Removed

of the seat. This loading arrangement provides an indication of the relative ultimate strengths of the various valves for a single load application and allows for the verification of the finite element model. This test method does not, however, include the effects of fatigue. Fatigue does play a major role in the failure of valves in the field but is beyond the scope of this study. Chapter 4 discusses the results of these tests as well as the results from strain gauge studies.

2.2 Failure Criteria

The materials used in the design of the valves are high strength brittle alloys. All valves are manufactured using powder metallurgy processes. Table 2.1 lists the material properties provided by the manufacturers as well as those assumed in this study. The values indicated with an asterisk in Table 2.1 are assumed values.

Table 2.1: Material Properties

| | Cast Cobalt | Tungsten Carbide | Nickel Carbide |
|---|-------------|------------------|----------------|
| Young's Modulus (E) | 151700MPa | 529500MPa | 586100MPa |
| Poisson's Ratio (ν) * | 0.3 | 0.3 | 0.3 |
| Ultimate Tensile Strength (σ_{ut}) | 690MPa | 2760MPa | 1930MPa |
| Ultimate Compressive Strength (σ_{uc}) * | 3100MPa | 12500MPa | 8700MPa |
| Hardness | 51-55 RWC | 87.5 RWA | 90.0 RWA |

* Indicates Assumed Value

2.2.1 Material Properties

Several assumptions had to be made regarding material properties. The valve manufacturers had very little data on the specific properties of the various materials. Literature searches revealed large variations (up to a factor of 2) in the strengths of similar materials having slightly differing chemical compositions. The material properties provided by the manufacturers are modulus of elasticity, ultimate tensile strength, and hardness.

A value of 0.3 was assumed for Poisson's ratio based solely on the fact that most metals have values near 0.3. A sensitivity analysis discussed in Section 5.1.2 showed that variations in stress levels within critical regions of the valves are small for large changes in Poisson's ratio.

The values used for the ultimate compressive strength are based on experimental data and model predictions as follows. In preliminary studies which assumed that the tensile and compressive strengths of the materials are equal, the finite element models predicted that failure occurs due to axial compression in the corner where the shoulder meets the lip. It was noted that the failures experienced in the lab and in the field appeared to be tensile failures due to hoop stresses in the lip region. Using the Coulomb-Mohr failure criterion, the value for the compressive strength was increased in the finite element models until tensile hoop stresses became the predicted failure mode. The lowest value for which tensile hoop stress failure was predicted was recorded. The values presented in Table 2.1 are, therefore, the minimum possible

compressive strengths of the materials. The actual values are likely even higher, however, with the information available, it is not possible to determine their values more accurately. This method of estimating the compressive strength did not involve specific strength testing as direct determination of material properties is not within the scope of this project. The manufacturer of the valves was unable to provide any indication of actual values. These values are, therefore, the best estimates of the actual compressive strengths possible under the given circumstances.

The values for the hardness are measured values. It is somewhat unfortunate that this is the only reliable information regarding the material properties of the valves. It is a property which is unrelated to the stress levels developed in the valves and, therefore, does not aid in this analysis. The hardness is used only for selecting which material should be used for a valve in a given well. The nickel carbide and tungsten carbide valves have a high hardness and are very good for abrasive environments. Although the nickel carbide is somewhat better than the tungsten carbide in terms of corrosion resistance, they are both relatively poor in this regard. The cast cobalt is very good in corrosive environments but, due to its lower hardness, does wear more easily than do the carbides.

2.2.2 Failure Criteria in Ansys

Initially, this axi-symmetric analysis was to be a small part of the research project. This section of the study became significantly more important when several failures began to occur in the field. A quick solution to this part of the research was desired in order to prevent further field failures.

Ansys offers two failure criteria, the VonMises criterion, and the Maximum Shearing Stress Yield criterion. Neither are appropriate for predicting failure of brittle materials. For the Maximum Shearing Stress Yield criterion (or the Tresca-Saint Venant Yield Hypothesis) failure is predicted when:

$$MAX(|\sigma_1 - \sigma_2|, |\sigma_2 - \sigma_3|, |\sigma_3 - \sigma_1|) > \sigma_Y \quad (2.4)$$

where σ_1 , σ_2 , and σ_3 are the principal stresses and σ_Y is the yield strength [11].

The VonMises criterion (or the Strain Distortion Energy criterion) predicts that failure will occur when:

$$\frac{1}{2}[(\sigma_1 - \sigma_2)^2 + (\sigma_2 - \sigma_3)^2 + (\sigma_3 - \sigma_1)^2] > \sigma_Y^2 \quad (2.5)$$

again with σ_1 , σ_2 , and σ_3 as the principal stresses and σ_Y as the yield strength [11].

These criteria are primarily used to predict yielding failure in materials with maximum tensile yield strength and maximum compressive yield strength having the same magnitude. The materials used in the valves do not yield and do not have the same magnitude for the ultimate tensile and compressive strengths. With the high compressive strengths of the materials used, these two criteria are highly conservative for compressive and mixed failures. Initially, an arbitrary choice was made to use the VonMises criterion.

In the early stages of this study, the VonMises criterion was used in part because preliminary studies were exercises to verify correct usage of the finite element methods, and also because no failure theories for brittle materials were available in Ansys. Consequently, early studies led to overestimation of stresses at a compressive stress concentration. Based on this analysis, it was deemed necessary to remove material in a large radius from the area where the shoulder and the lip meet to relieve the stress concentration at that location. Testing was performed on valves with this undercut in the shoulder region. For the purposes of comparison with these tests, models including the undercut have been maintained throughout the analysis even though the modification is now understood to be unnecessary.

2.2.3 Coulomb-Mohr Failure Criterion

As it became obvious that this study was becoming vital, it was necessary to choose a more appropriate failure criterion. The Coulomb-Mohr failure criterion is specifically used for brittle failure prediction [1, 2]. This criterion requires knowledge of the ultimate compressive strength (σ_{uc}) and the ultimate tensile strength (σ_{ut}). Two circles

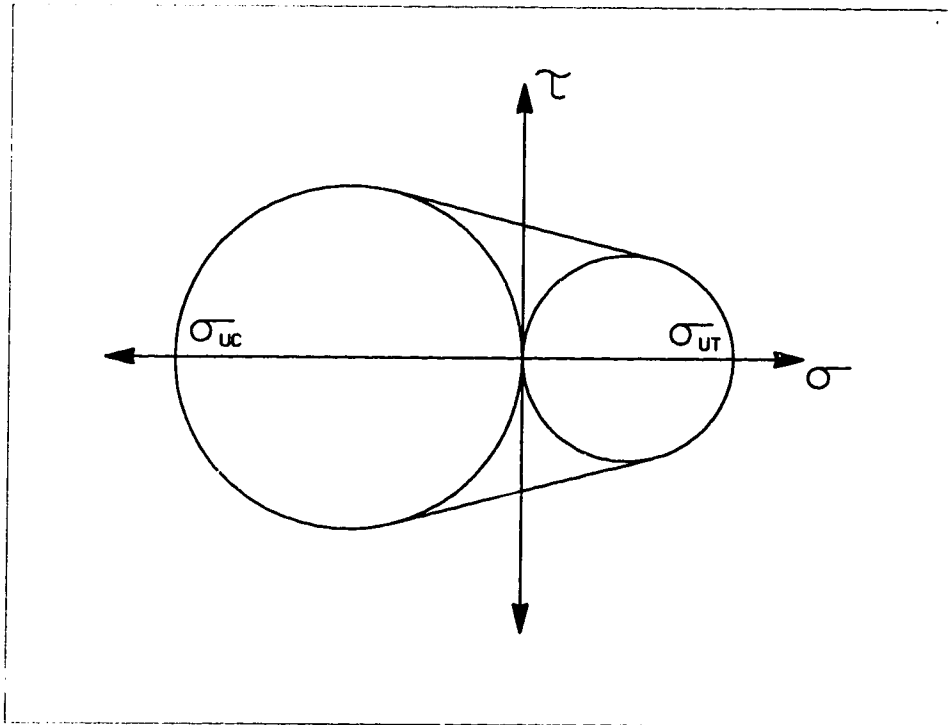


Figure 2.3: Coulomb-Mohr Failure Criterion - σ vs. τ

are drawn on a Mohr diagram representing uniaxial tension and uniaxial compression failure tests. Tangent lines are drawn between the circles as in Figure 2.3. Failure is predicted if the stress at any point in the body lies outside of the region bounded by the two circles and the tangent lines. A diagram such as the one in Figure 2.4 is drawn to represent this failure criterion in terms of σ_1 and σ_3 . Failure occurs, again, when the state of stress lies outside of the polygon. The locations 'A' represent possible states of stress in excess of the failure limit for each of the three failure modes. In the top right quadrant, both σ_1 and σ_3 are in tension and failure is based on the value of σ_1 . In the lower right quadrant, σ_1 is in tension and σ_3 is in compression. Failure here is based on the values of both σ_1 and σ_3 . In the lower left quadrant, both σ_1 and σ_3 are in compression and failure is based on the value of σ_3 . The locations 'B' represent the state of stress at which failure would initiate given the state of stress at 'A'. The ratio of the length of the dotted line to point 'A' over the length of the line to point 'B' gives an indication of how close a certain state of stress is to failure. Failure is

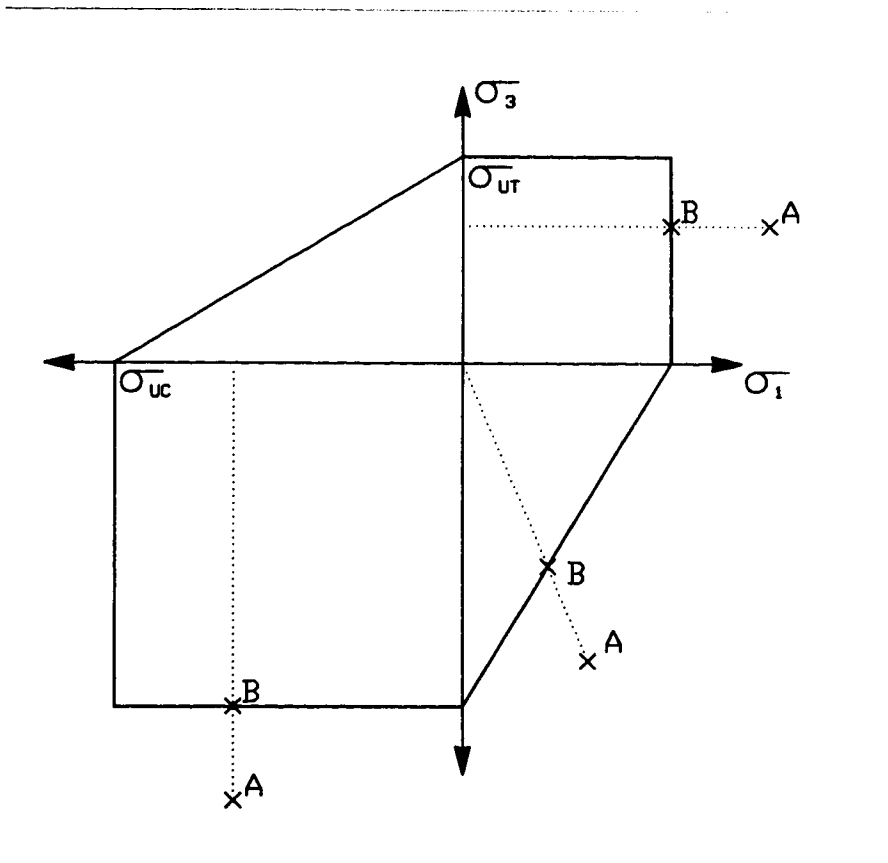


Figure 2.4: Coulomb-Mohr Failure Criterion - σ_1 vs. σ_3

predicted when the ratio is greater than 1. This failure criterion is not available within Ansys so it was necessary to write code in the Ansys Parametric Design Language. The input required for the code is the ultimate compressive and tensile strengths of the material as well as the principal stress data at each node. Table 2.2 shows equations which express the ratio between the actual state of stress at a given point in the body and the associated stress at failure. In these equations, σ_{uc} is expressed as a negative

Table 2.2: Coulomb-Mohr Failure Criteria

| Stress State | Failure Criteria |
|------------------------------|---|
| $\sigma_1 > \sigma_3 > 0$ | $\frac{\sigma_1}{\sigma_{ut}} > 1$ |
| $0 > \sigma_1 > \sigma_3$ | $\frac{\sigma_3}{\sigma_{uc}} > 1$ |
| $\sigma_1 > 0, \sigma_3 < 0$ | $\sigma_3 / \left(\frac{\sigma_{ut}}{(\sigma_{ut}/\sigma_{uc} + \sigma_1/\sigma_3)} \right) > 1$ |

(ie. compressive) value. The code uses the equations in Table 2.2 to generate this Coulomb-Mohr Stress Ratio for every node. The results are plotted as contour plots which can be used to predict where failures will initiate. Many of the contour plots presented later are based on this code.

2.3 Observed Failures

Failures observed in the field are different in nature compared with the failures created in the lab. In the field, the effects of fatigue result in failures typically limited to the upper ring of the valve whereas in the lab, the failures propagate throughout the body. While the initiation site remains consistent between the two failure modes, the load at which failure occurs and the way in which these failures propagate are quite different. Valves in the field tend to fail at loads far below the loads applied in the lab. Fatigue lowers the value of the peak load that the valves are able to withstand. Propagation of failures in the field occur over several load cycles until part of the lip is broken off from the upper portion of the seat. In the lab, failures are sudden and usually result in the seat breaking into many fragments with much energy.

2.3.1 Field Failures

Unlike failures produced in the lab, failures in the field are affected by environmental conditions. Often the fluid is very acidic resulting in a weakening of the valve due to corrosive wear. Other times, the environment contains impurities such as sand or silt. This greatly increases the abrasive wear of the valves. The combination of abrasive and corrosive environments has caused some valves to fail in as little as two days of service. Other valves in less hostile environments are still pumping effectively after two years of service. It is beyond the scope of this study to deal with the effects of corrosion and wear resistance.

Since the wells are not continuously monitored, a broken valve may not be detected for days after the initial failure has occurred. When this occurs, failures keep propagating through the valve with the continued loading and unloading and more pieces of the lip can break off. In such cases, determination of the cause of initial failure is very difficult.

Figure 2.5 shows a series of valves which have been broken in service, indicating the variation in the extent of damage often observed. The valve shown on the left with almost none of the upper ring left intact was left in a well still running for a long time after the initial failure occurred. This resulted in the fracture surfaces actually being polished by the fluid wash. Models using the VonMises failure criterion indicate the top of the lip and the inside edge of the shoulder as being a high stress regions. The valves shown in Figure 2.5 are not useful in determining which of these locations is the initiation site of the failures. The failures extend through both high stress regions (ie. the inside edge of the shoulder where it meets the upper lip and the upper inside corner of the lip itself).

The location of the point at which the failures initiate was not known until a sales representative for the valves' distributor noticed a small crack in one of the valves that had been in service but had not yet completely broken. The pump including this valve was out of the ground for maintenance unrelated to the valves. Figure 2.6 is a picture of this valve in which dye penetrant was used to indicate the pattern of the cracking.

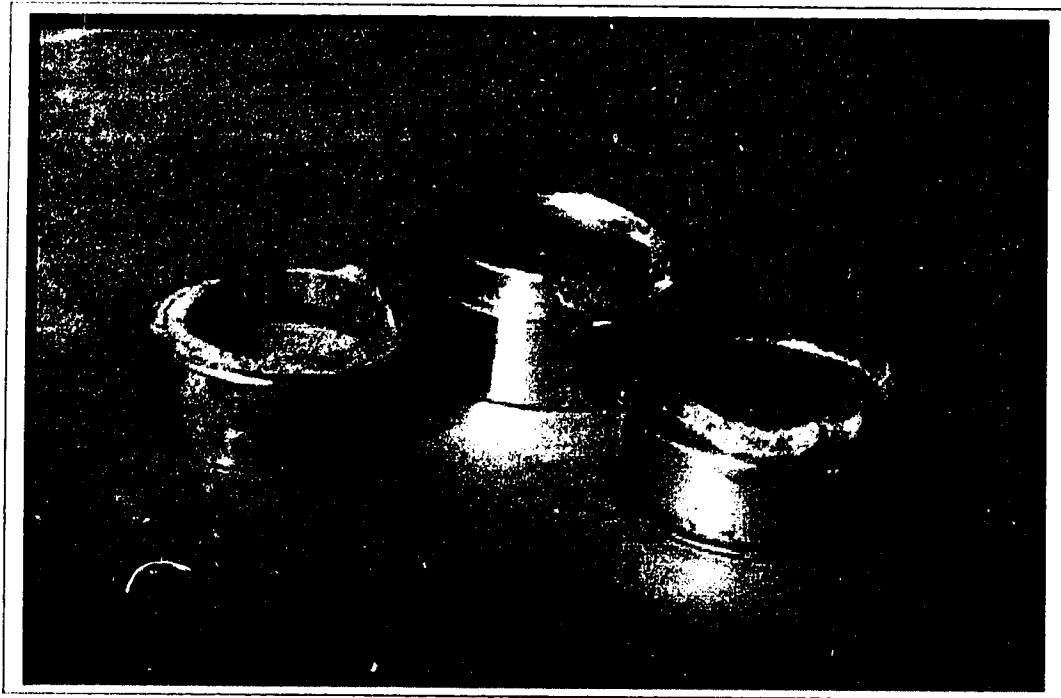


Figure 2.5: Three Valves Broken In Service

The lines are regions in which the dye has come back out of the cracks into the white chalk placed on the surface of the valve. This valve indicates that the failures initiate from the upper lip of the seat and propagate down. Along the inside edge of the seat, about one third of the way down, the cracks then propagate horizontally. The initial vertical crack eliminates the seat's ability to support hoop stresses, therefore, outward bending of the upper lip is increased. Tensile axial stresses develop along the inside edge of the seat because of this outward bending and are the cause of the horizontal crack propagation. This horizontal crack then propagates radially through the body until the upper lip becomes detached and breaks away. As will be seen in Section 3.2, this evidence supports the use of the Coulomb-Mohr Failure Criterion which correctly predicts the top inside corner of the lip as the source of the failures.

2.3.2 Lab Failures

In a typical field failure only a small piece breaks off of the seat, usually in the lip region. In the lab, the fractures propagate very differently. For valves made from cast

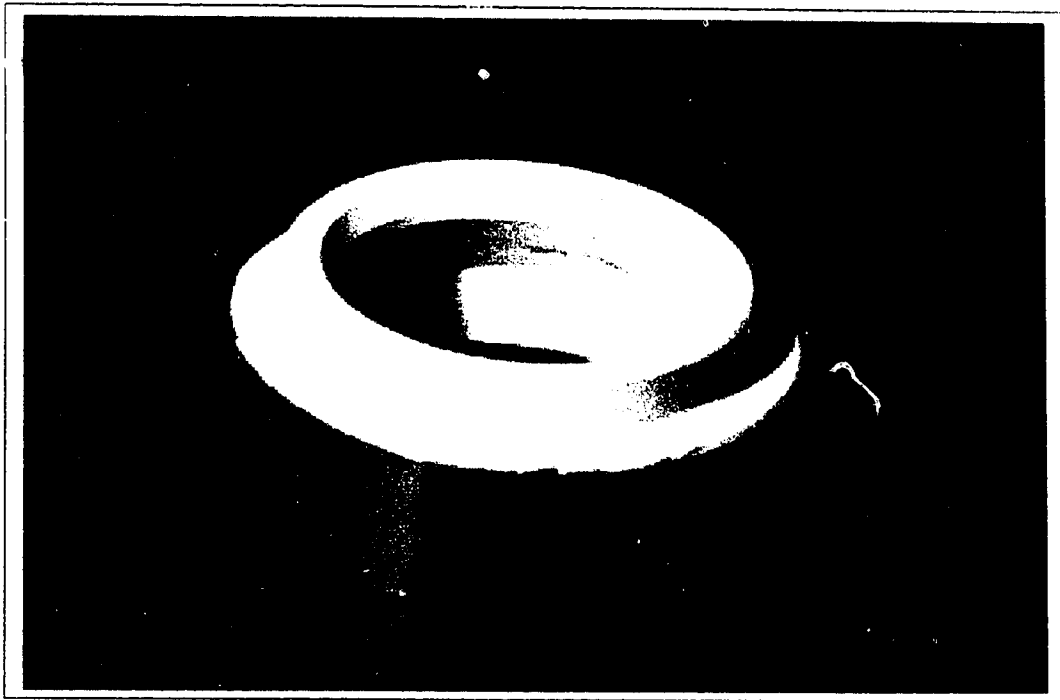


Figure 2.6: Cracked Valve Shown With Dye Penetrant

cobalt the valves break into an average of three large pieces characterized by vertical fracture surfaces extending from the initiation site near the top of the lip (similar to the field failures) through to the base of the seat without turning horizontal as described for the field failures in Section 2.3.1. This lab failure can be seen in Figure 2.7. For the carbide materials the lab failures are much more dramatic. The seats typically fracture into dozens of small pieces as in Figure 2.8. In both cases the failures are sudden and violent. Protective shields were necessary around the testing equipment to prevent injury to people in the lab and damage to other equipment from the shrapnel. In one test, a carbide fragment had enough energy to penetrate a 3 mm thick lexan sheet being used as a shield. The large difference in the failure modes between the field and the lab emphasize the fact that the lab data can be used only for relative comparisons between different designs. The data collected is not useful to predict the allowable pressure for loading in the field.



Figure 2.7: Lab Failure of a Cast Cobalt Valve

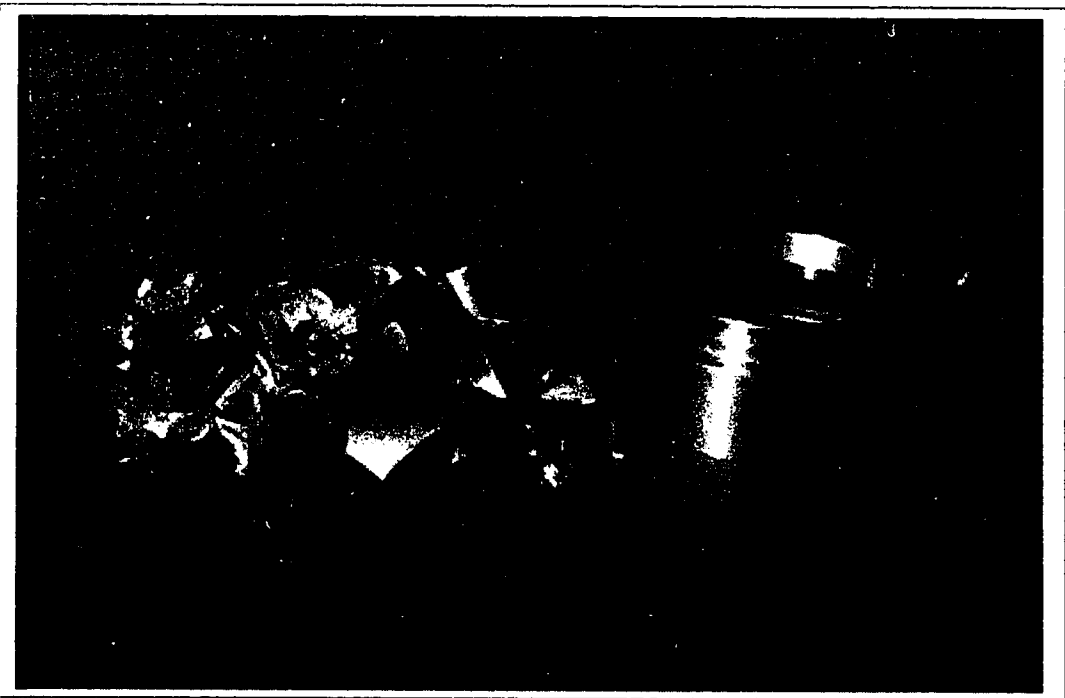


Figure 2.8: Lab Failure of a Nickel Carbide Valve

Chapter 3

Frictionless Contact Modeling

3.1 Finite Element Meshing

All finite element models used in the analysis of the behavior of these valves use two dimensional, axisymmetric, four node quadrilateral and three node triangular elements (triangular elements are used scarcely in areas of element size transition). Figure 3.1 is a plot of a typical mesh. Pictured is a two inch, nickel carbide, modified with undercut valve.

3.1.1 Element Selection and Mesh Density

Four node quadrilateral elements were chosen versus eight node quadrilateral elements because of the shorter convergence times required. Differences in convergence times are a function of the total number of nodes in the body. The advantage of the eight node element is that the mid-side nodes add eight more degrees of freedom per element. The elements, then, are far more flexible and result in a more realistic model. It was found, however, that the relative change in the peak stress values for several models tested with the eight node elements was less than 2% versus similar four node element models. It was felt that this small change did not warrant the expense of doubling the necessary convergence times.

The mesh density is higher in the contact region and in the upper lip where the

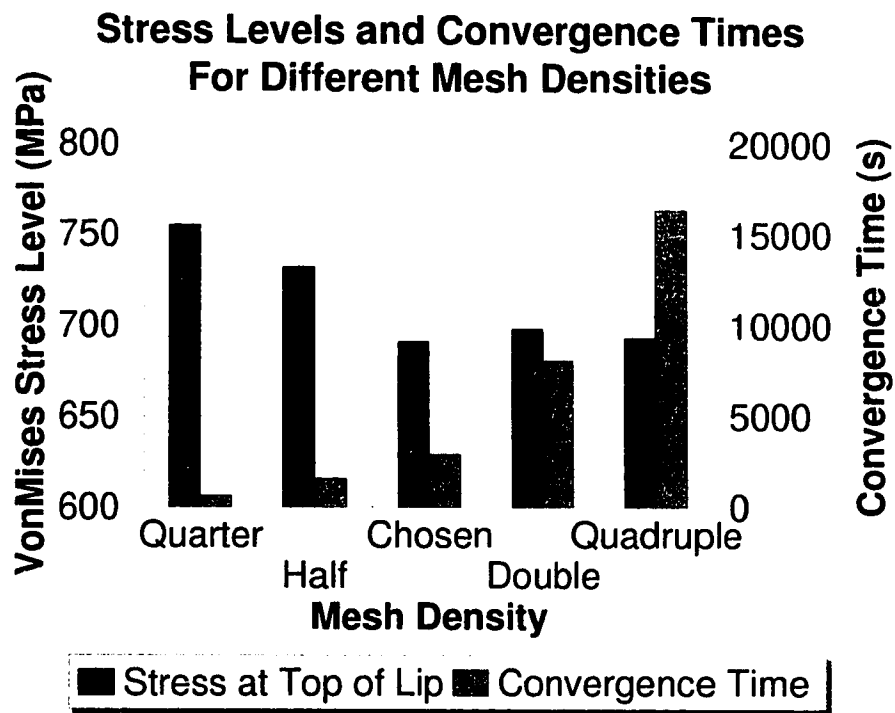


Figure 3.2: Effects of Changes in Mesh Density on a 2" Nickel Carbide Valve

3.1.2 Contact Elements

Contact between the ball and the seat is modeled using two dimensional point to surface contact elements meshed symmetrically across both contacting surfaces. Point to surface elements were chosen versus point to point elements due to the relatively large transverse displacements of the two surfaces compared to the size of the elements (Transverse deflections are on the order of 2 element widths). Point to point contact elements are better suited for contact with little transverse deflection and where the nodes line up reasonably well across the two surfaces [11]. In symmetric meshing, the elements are generated twice. The second time the elements are generated, the contacting surface that had the element ‘points’ the first time has the element ‘surfaces’ the second time and vice versa. This results in two sets of contact elements over-lapping each other. A discussion of the benefits of symmetric meshing versus asymmetric meshing (ie. not generating the second set of elements) is discussed in Section 5.1.3.

The coefficients of friction are not known for the various materials used in the valves. In the initial models, the contact elements were given a value of zero for the coefficient of friction. In later models, as described in Chapter 5, the values of the coefficients of friction were inferred from the destructive test data as outlined in Section 5.2.

3.2 Initial Guided Stem Design

The guided stem design concept for the new valves was innovative and progressive, however, the product was introduced into service without the benefit of engineering design and testing. Prior to this study, trial and error was the dominant tool used by the original designers of the valves to determine what modifications needed to be implemented to improve the design of failing valves. This research project was initiated to get an engineering perspective of the guided stem design and to modify that design to reduce the number of failures occurring in the field. An understanding

of the basic mechanics of the contact between the ball and the seat was sought mainly through finite element modeling. No literature could be found describing a solution of what is essentially an elastic contact between a sphere and the inside surface of an inverted cone. This solution was desired to test the validity of the finite element models.

Figure 3.3 is a quarter section view of the guided stem design showing the simulated hydrostatic pressure distribution used in the models. The pressure distribution represents the loading that results from lifting the column of oil. Pressure is applied across the top of the ball and down the side to the point of contact. Below the point of contact exists a vacuum which draws the oil up from below. Pressure is exerted on the surface of the seat from the point of contact around to the edge of the shoulder. The shoulder is in contact with a ledge on the inside of the barrel and forms a seal. A quarter section view showing the preload applied to the shoulder resulting from this contact can be seen in Figure 3.4. This preload is, again, the result of the nose being tightened into the barrel, compressing the shoulder of the seat into the ledge on the inside of the barrel. The constraints shown on the bottom edge of the seat are the same for all models presented in this thesis. They consist of a vertical displacement constraint and a rotational constraint about the z axis.

Figure 3.5 and Figure 3.6 are plots of the stress distribution within the valve ball based on the VonMises and Coulomb-Mohr failure criteria respectively. Plots based on the VonMises criterion indicate the equivalent stresses in the body based on Equation 2.5. Plots based on the Coulomb-Mohr criterion indicate a ratio between the state of stress in the body and the associated stresses at failure using the equations in Table 2.2. The loading in both figures is that of the hydrostatic pressure only on a 2 inch nickel carbide valve. The stress distribution for the load case with both the preload and the hydrostatic pressure can be seen in Figure 3.7 which uses the Coulomb-Mohr stress ratio. It is evident that there is very little difference in the stress distribution between the two load cases in Figure 3.6 and Figure 3.7. The peak Coulomb-Mohr ratio only changes by 0.1%. Including the preload in the finite element models is, therefore,

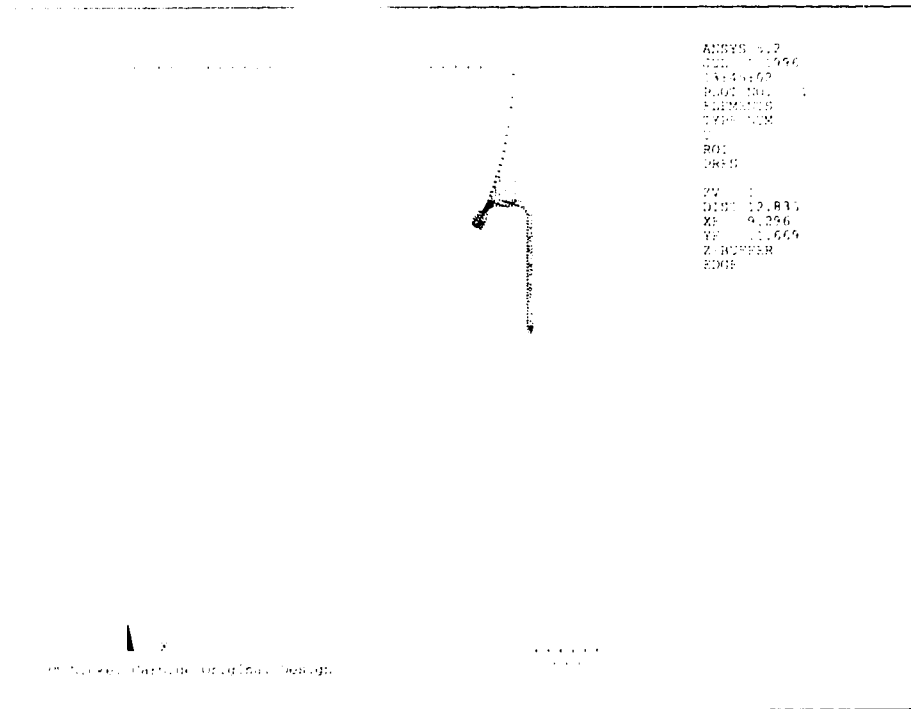


Figure 3.3: Loading Due to Hydrostatic Pressure

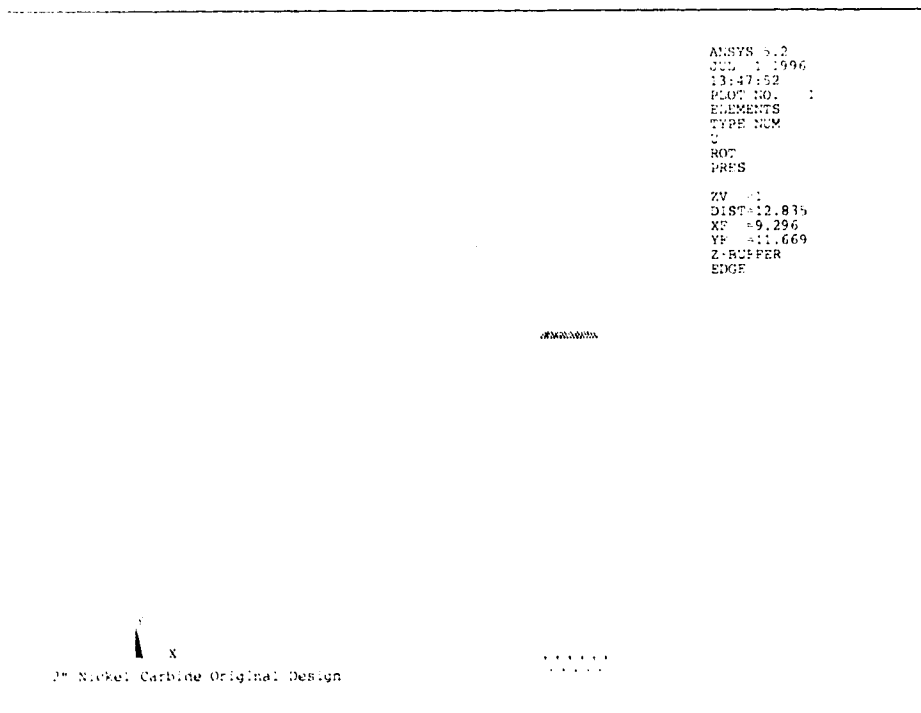


Figure 3.4: Loading Due to the Preload

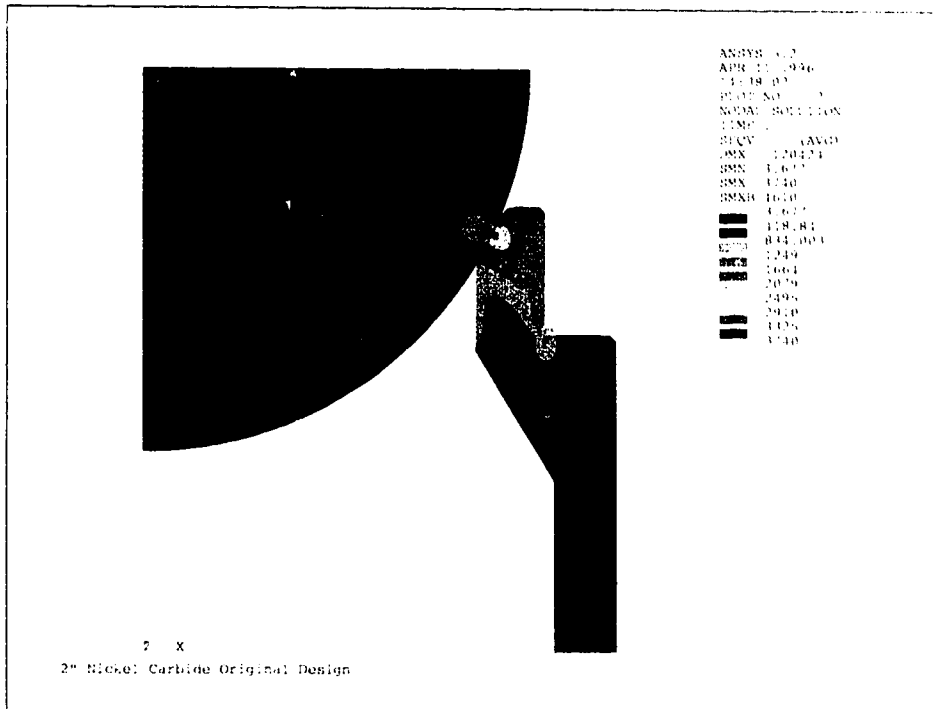


Figure 3.5: VonMises Distribution, 2" Nickel Carb. Original Design

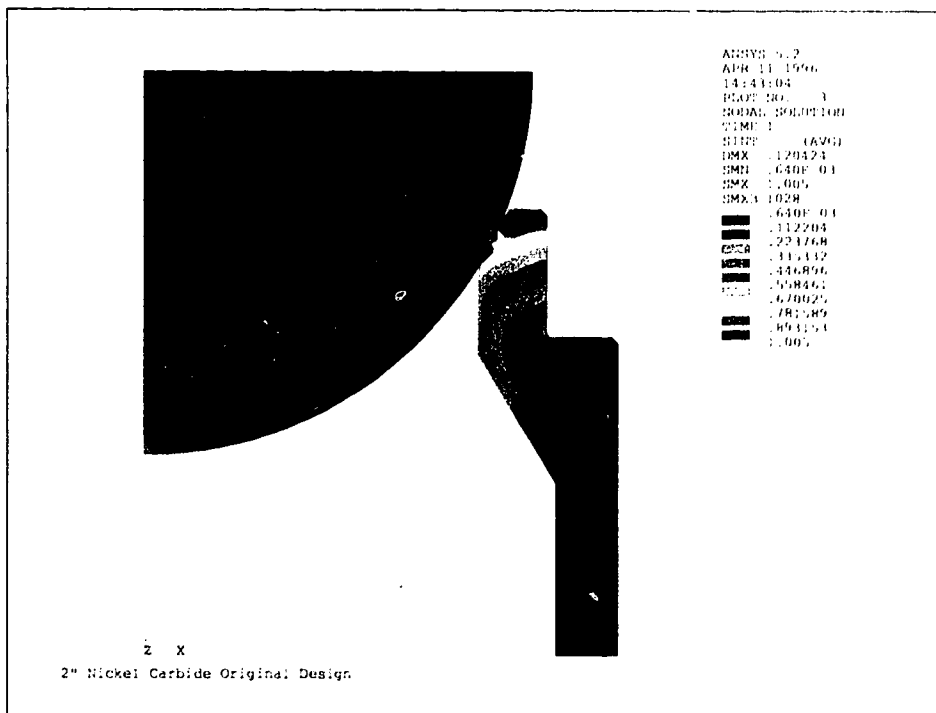


Figure 3.6: Coulomb-Mohr Ratio, 2" Nickel Carb. Original Design

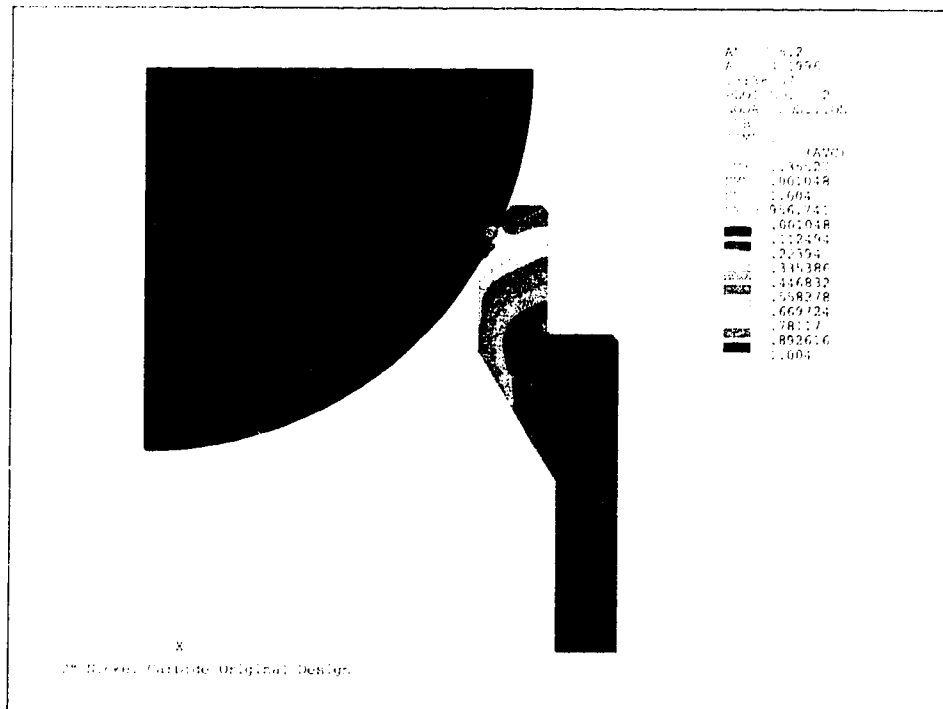


Figure 3.7: Coulomb-Mohr Ratio Including the Preload

unnecessary. It is not included in any further analyses.

Using the Coulomb-Mohr criterion as in Figure 3.6 there is only one high stress region. Failure is predicted to start from the top inside edge of the lip. Tensile hoop stresses are the dominant stresses in this region and, as such, one would expect to see vertical cracks propagate down from the upper lip. Observations from actual failures indicate that this prediction is correct. Using the VonMises criterion as in Figure 3.5 leads to an erroneous conclusion with regards to the initiation of failure. This criterion predicts failure will occur where the upper lip meets the inside edge of the shoulder. Figure 3.8 is a close up view of this region showing the stress concentration in the corner. This view is about a 15 times magnification of Figure 3.5. A secondary high stress zone is in the region of contact. Since there was insufficient information in the early stages of this project to use the Coulomb-Mohr criterion, all the modifications to the design were based on the results gathered from the VonMises criterion. The prediction of failure initiating in the corner of the shoulder was not considered unreasonable. In all of the observed failures, the lip had been broken off and the fracture



Figure 3.8: Closeup of Stress Concentration using VonMises Criterion

surface ran along the region where the lip met the shoulder. The small radius in the corner where the shoulder meets with the lip results in a stress concentration of primarily the axial compressive stresses. The compressive strengths of the materials used are much higher than the tensile strengths. The VonMises criterion does not take this into account and as such, this stress concentration is really not the concern that the VonMises criterion would indicate.

3.3 Modifications to the Seat Design

A limiting constraint regarding the modification of the valve design is that any changes must be made to the existing valves already manufactured. This means that the only changes possible are those that can be accomplished by way of material removal. A secondary constraint is an economic one. The materials used are very hard and, therefore, cannot be machined but rather must be modified using diamond wheel grinding. This is a relatively time consuming and expensive process. It also limits the types of modifications that can be made.

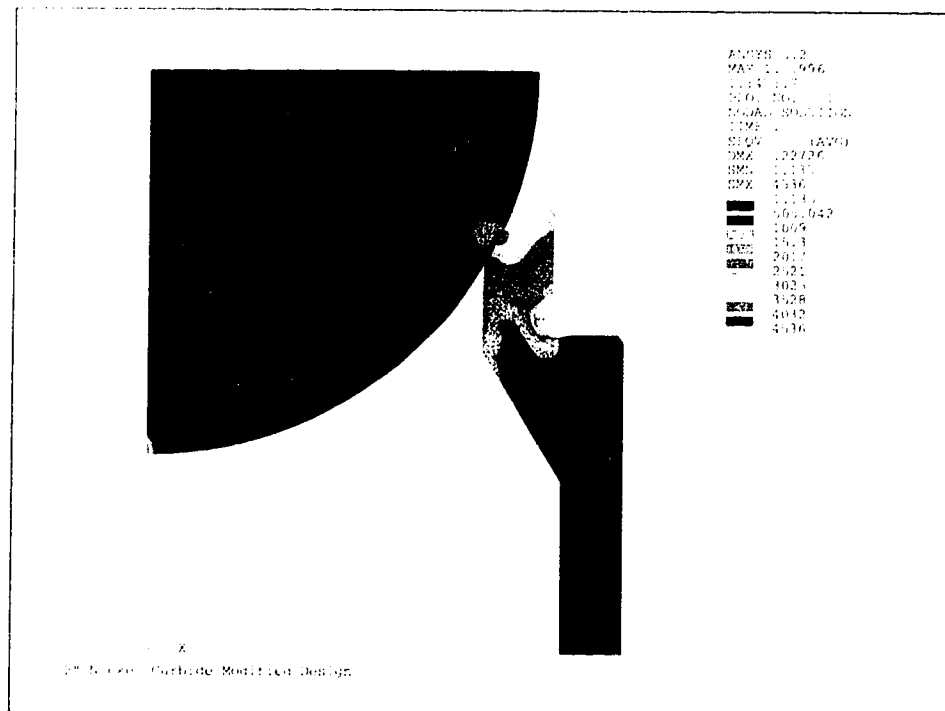


Figure 3.9: VonMises Distribution Showing Undercut to Shoulder Region

3.3.1 Undercut Shoulder

The stress concentration in the corner between the shoulder and the lip as shown in Figure 3.8 is caused by a tight radius. Due to different grinding procedures, the carbide valves have a tighter radius than do the cast cobalt valves. This increases the effect of the stress concentration in the carbide valves. Using the VonMises criterion, it was felt that increasing the radius was necessary to remove this stress concentration. To accomplish this, the corner was ground back (undercut) as in Figure 3.9. This modification was considered unnecessary for the cobalt valves because of the larger initial radius and, therefore, lowered stress concentration. Figure 3.9 is a plot of the stress distribution using the VonMises criterion for a 2" nickel carbide valve with this modification. Comparing this with Figure 3.5 it is obvious that this modification actually increases the peak stress levels by about 21%, based on the VonMises criterion. Figure 3.10 is a plot of the same model using the Coulomb-Mohr criterion instead of the VonMises criterion. Comparing Figure 3.6 and Figure 3.10 it is evident that the

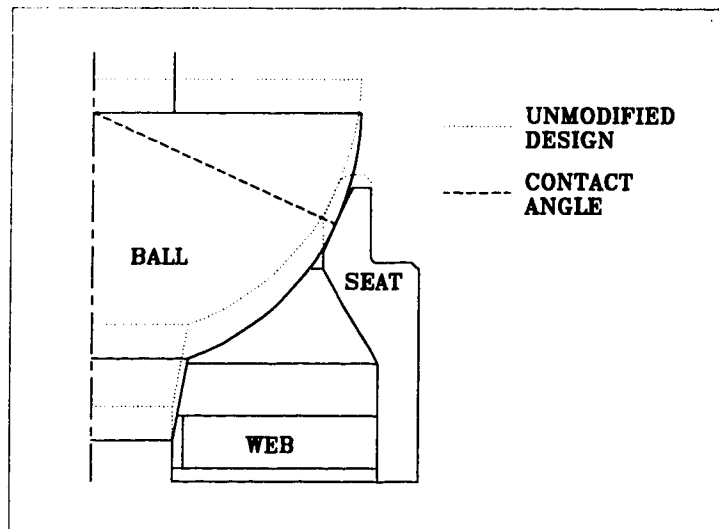


Figure 3.11: Quarter Section Drawing Showing Lowered Point of Contact

3.3.2 Lowered Contact Point

It was expected that the stresses in the shoulder area would be reduced if the point of contact was brought deeper into the body of the seat. There are two reasons for this. The vertical distance between the point of contact and the shoulder is reduced, thereby, reducing the effective moment arm of the radial component of the reaction force to the bottom of the lip. Because of this decrease in leverage there is less bending of the upper lip and, therefore, a decrease in the stress levels. Secondly, the reaction force is in the thicker portion of the seat. The distance that the contact point can be lowered is limited by the web across the bottom of the seat. It is necessary to maintain the point of contact high enough such that the ball does not come in contact with the web, accounting also for wear allowances. Figure 3.11 illustrates this modification.

Figure 3.12 and Figure 3.13 are stress distribution plots of a model having the lowered point of contact using respectively the VonMises and Coulomb-Mohr criteria.

When these plots are compared with Figure 3.5 and Figure 3.6 reductions of the peak stress levels of 22% using the VonMises criterion and of 9% using the Coulomb-Mohr criterion are evident. Stresses in the shoulder region are decreased partly because the outward bending is reduced but also because the axial component of the reaction force

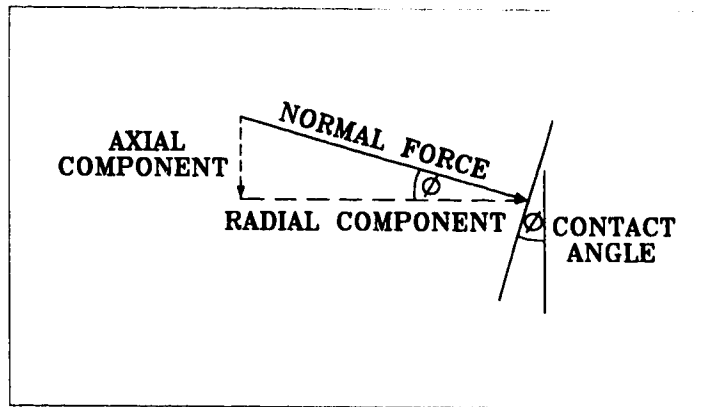


Figure 3.15: Effect of Contact Angle on Reaction Force

less material to make each seat due to the elimination of the lip are outweighed by the decrease in strength and, as such, this modification was no longer considered.

3.3.3 Increased Contact Angle

Further reduction of the outward bending of the seat and, therefore, reduction in the hoop stresses can be accomplished by reducing the radial component of the reaction force. Since the valves are axisymmetric, the radial components of the fluid pressure on the ball have little effect on the total loading of the valve as they cancel each other out. The vertical components of the applied pressure on the ball can only be balanced by the reaction force between the ball and the seat. The vertical component of the reaction force, then, is constant for any given pressure and balances the vertical pressure differential across the ball. Changing the contact angle ϕ , between the ball and the seat will change the magnitude of the normal reaction force and, therefore, the radial component of the reaction force. Figure 3.15 shows this relationship between the contact angle ϕ and the reaction forces. Decreasing ϕ , thus making the contact angle steeper, will result in an increase in the magnitude of the normal force and, therefore, an increase in the radial component of this force. Increasing ϕ to make the contact surface flatter, or more horizontal, will decrease the radial component of the reaction force which is the goal of this modification. The extent to which the contact angle can be changed is limited by the inside diameter of the seat and the radius of

the ball. For any given contact angle there is a circle on the ball that has a slope equal to that angle. Contact is made on this circle. As the angle ϕ is increased, the radius of this circle decreases. When changing the contact angle it is necessary to maintain the radius of the contacting circle to be greater than the inside radius of the seat. If the circle becomes too small, the surfaces will not contact properly. The radius of this circle must also be large enough to prevent the small changes in geometry from valve to valve due to manufacturing tolerances from affecting the quality of the contact and thus the sealing capacity of the valve. The contact angle was chosen for each valve size such that the contacting radius is 0.6mm larger than the specified inside radius of the seat. Table 3.1 lists the original and modified contact angles as well as the distance that the contact surface was lowered (as described in Section 3.3.2 for each valve size).

Table 3.1: Modifications to Contact Angle and Height of Contact Point

| Size | Old Contact Angle | New Contact Angle | Distance Contact Point Lowered |
|-------------------|-------------------|-------------------|--------------------------------|
| 1 $\frac{1}{4}$ " | 14.5° | 19.0° | 1.61mm |
| 1 $\frac{1}{2}$ " | 23° | 25.2° | 1.65mm |
| 1 $\frac{3}{4}$ " | 25° | 25.2° | 5.14mm |
| 2" | 25° | 27° | 2.28mm |
| 2 $\frac{1}{4}$ " | 25° | 26° | 1.15mm |

A plot of the stress distribution, using the Coulomb-Mohr criterion, of a valve with the altered contact angle and the lowered contact point can be seen in Figure 3.16. When this is compared with the plot of the model without the altered contact angle in Figure 3.13 it is obvious that the stress levels have again been reduced significantly. The modifications as shown in Figure 3.16 represent the final modified design. Table 4.1 in the next chapter can be used to compare the predicted (frictionless) and actual loads at failure for both the original design and the modified with undercut design in all three materials and in all five sizes. Table 5.3 compares the predictions that include friction to the predictions that do not include friction.

Chapter 4

Lab Testing

Initially, testing was not within the scope of this thesis. After some preliminary models showed encouraging results, a limited number of tests were conducted to verify these results. Two different types of testing were done in the lab. The first was a straight load to destruction test. The second was a strain gauge study initiated due to interesting results found during the destructive tests.

4.1 Destructive Testing

When the modified with undercut design was proposed, load tests on thirty-four different valves were performed. These valves included all the combinations of the three materials, and the five sizes, with modifications and without. The four extra valves were for repeated tests which included strain gauges to collect more data. For comparison against the API design, one tungsten carbide valve in each of the five sizes was purchased from a competitor to be subjected to the same test. The results of the API tests are not presented here, however, it can be said that the results were comparable to those for the modified valves.

4.1.1 Test Setup

A true test of the valves is to subject them to hydrostatic loading as they would experience in a well. In the lab, such a test would be complex and expensive. The effects of fatigue are not being studied, therefore, a single load to failure test is sufficient. The load at which the valves fail using a single load is considerably higher than for valves experiencing cyclic loading. This means that the pumps and associated equipment would have to be able to withstand the substantially higher loads themselves. It is possible that the housings may fail before the valve at those elevated pressures. Building special housings and acquiring large enough pumps would be quite expensive. The labor involved with disassembling and reassembling the equipment for every test would also be very time consuming.

A simpler means was desired to simulate the loading on the valves. The net force of the hydrostatic pressure is directed vertically. In the test method chosen, a mechanically applied vertical load was used to simulate the load on the valves. Finite element models were made using a distributed pressure load across the top of the ball to simulate the testing conditions. No pressure was included on any surface other than the top of the ball. Results from these models show that the radial components of the hydrostatic pressure do have some effect on the final solution but their influence is small compared to the reaction load between the ball and the seat due to the vertical components of the pressure. Because of the axisymmetry of the valves, radial components of the pressure are self-equilibrating. As such, these loads only have localized effects on the valves. The mechanically applied vertical load is, then, an acceptable simulation of the hydrostatic loading.

An Instron universal testing machine was used to apply the load to the valve. A load cell with a capacity 22500 N was used for measuring the applied loads. A steel plate was placed on the base of the Instron to prevent the valve from indenting the surface of the testing machine. The ball and seat of the valve were placed on the steel plate. To achieve a uniformly distributed load across the top of the ball, it was necessary to remove the stem from a ball in each of the five sizes. For economic

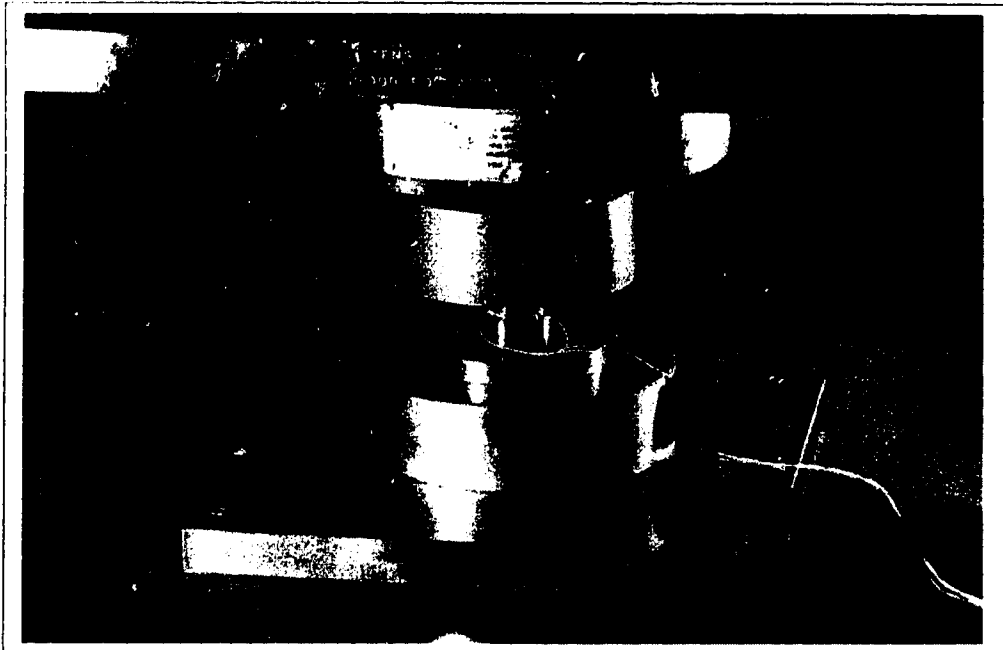


Figure 4.1: Picture of Compression Test Setup

reasons, only one cast cobalt ball in each size had the stem removed. These five balls were also used with the tungsten carbide and nickel carbide seats. This modification was shown earlier in Figure 2.2 for the two inch valve size. The strain gauge shown was placed to measure hoop strain, the dominant strain in the lip region. Another steel plate was placed on top of the flat surface of the ball to prevent the valve from indenting the surface of the load cell. To begin the test, the cross head was brought down until the base of the load cell initiated contact with the upper steel plate. This arrangement can be seen in Figure 4.1 and closer to the valve in Figure 4.2. The cross head was then lowered at a rate of 0.127mm/minute, thus applying an increasing, vertical compressive load to the valve. For all the tests, the contacting surfaces on the ball and seat were lubricated with motor oil to better simulate the frictional conditions that the valve would experience when in service. The test was continued until failure of the valve occurred. Failure of the valves featured breakage into many pieces, often with great energy release. For this reason, a 3 mm thick sheet of lexan was made into a cylinder approximately 20cm in diameter and 15cm tall. This ring was placed around the valves being tested to contain the debris. Even with the barrier in place

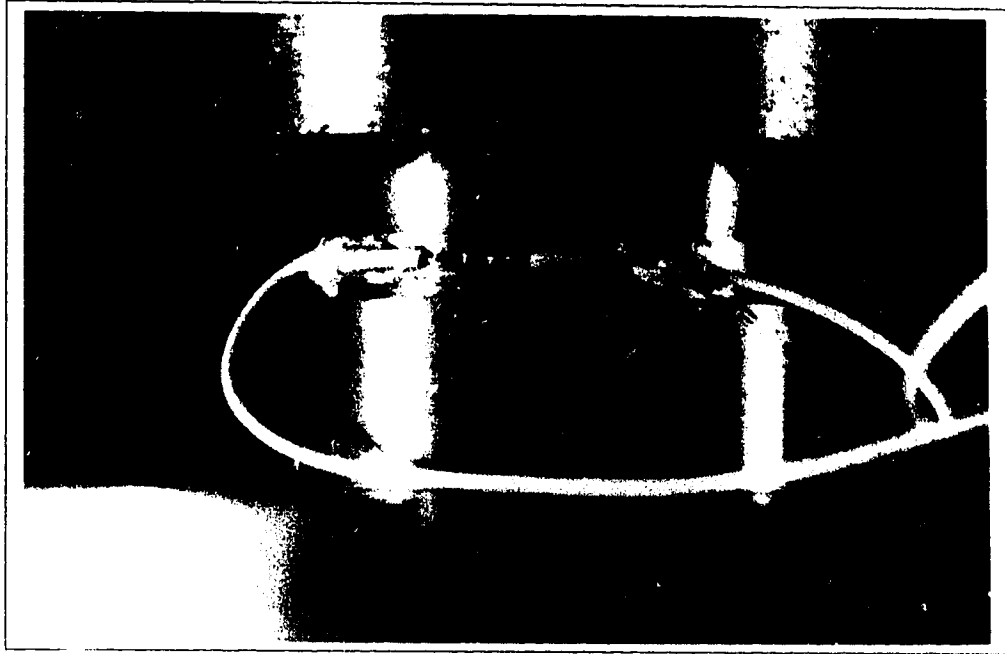


Figure 4.2: Close Up Picture of Valve In Compression Test

several fragments were still able to escape so safety glasses and plywood barriers were also used.

4.1.2 Test Results

The data collected consisted of the axial load applied to the valve by the crosshead and, in some cases, the hoop strain found on the outside of the upper lip of the seat. Strain gauges were placed on the tungsten carbide and cast cobalt valves in the 2" and the 2 $\frac{1}{4}$ " sizes as described later in Section 4.2.1. Due to the high cost of the destructive tests, only four valves were gauged. The nickel carbide valves were not gauged because it has similar properties to the tungsten carbide. It is less difficult to affix strain gauges to the larger sizes, therefore, the 2" and the 2 $\frac{1}{4}$ " valves were chosen to be gauged over the other sizes. The data collected from the strain gauges was used to determine the coefficient of friction in the next phase of the study as described in Section 5.2. The loads at failure of all the valves and the associated frictionless finite element predictions are presented in Table 4.1.

Table 4.1: Frictionless Predictions and Actual Loads at Failure

| Size | Predicted (N) Original Design | Predicted (N) Modified w/ Undercut | Actual (N) Original Design | Actual (N) Modified w/ Undercut |
|--|-------------------------------------|--|----------------------------------|---------------------------------------|
| Tungsten Carbide | | | | |
| 1 $\frac{1}{4}$ " | 32170 | 57075 | 72460 | 132150 |
| 1 $\frac{1}{2}$ " | 68220 | 116395 | 48750 | 171700 |
| 1 $\frac{3}{4}$ " | 162260 | 204960 | 84605 | 218185 |
| 2" | 124040 | 210140 | 80470 | 202215 |
| 2" gauged | Same | Same | 118365 | 220120 |
| 2 $\frac{1}{4}$ " | 296900 | 439410 | 172455 | * 285400 |
| 2 $\frac{1}{4}$ " gauged | Same | Same | 206440 | * 344470 |
| Nickel Carbide | | | | |
| 1 $\frac{1}{4}$ " | 20755 | 37150 | 40280 | 70725 |
| 1 $\frac{1}{2}$ " | 45355 | 116395 | 78445 | 126730 |
| 1 $\frac{3}{4}$ " | 105325 | 133795 | 100350 | 178420 |
| 2" | 78805 | 111640 | 87850 | ** (222410) |
| 2 $\frac{1}{4}$ " | 188430 | 281065 | 189830 | * 302770 |
| Cast Cobalt (Undercut Not Included In Modification) | | | | |
| 1 $\frac{1}{4}$ " | 9340 | 21375 | 16750 | 44615 |
| 1 $\frac{1}{2}$ " | 18061 | 47560 | 27225 | 61210 |
| 1 $\frac{3}{4}$ " | 41560 | 60635 | 43795 | 87610 |
| 2" | 32105 | 65670 | 39835 | 73640 |
| 2" gauged | Same | Same | 36965 | 60650 |
| 2 $\frac{1}{4}$ " | 76800 | 102925 | 65810 | 88075 |
| 2 $\frac{1}{4}$ " gauged | Same | Same | 72240 | 89385 |

* Using a Different Testing Apparatus with a
Higher Load Capacity

** Sample Broke While Unloading After Reaching
222410 N (50000 lb) Load Limit of Testing Machine

For most brittle materials, tests on macroscopically identical test coupons reveal some degree of scatter for the load at failure [4]. It can be reasonably assumed that this will be the case for all three materials used in the valves. The only comparisons that can be made to confirm this are between the gauged valves and their respective ungauged valves. The maximum variation observed was 32% between the 2" tungsten carbide valves. The minimum variation observed was 1% between the 2 $\frac{1}{4}$ " cast cobalt valves. The average variation for the tungsten carbide valves was 18% while the average variation for the cast cobalt valves was 9%. The samples are obviously too small for effective conclusions to be drawn regarding the range of results. They do, however, give an indication that there is likely a significant degree of scatter associated with the data collected.

The nickel carbide valves showed very similar failure loads to the tungsten carbide valves. This is an interesting result in that the tensile strength of the nickel carbide is reported as 1930 MPa and that of tungsten carbide as 2760 MPa. By these numbers, the failure loads for the nickel carbide valves should be approximately two thirds those for the tungsten carbide valves. The finite element analysis confirmed these predictions. The specified surface finish and geometry is the same for the valves in both materials and the Young's Moduli differ by only 10% so this similarity in failure loads is unexpected.

The relative increase in the load at failure due to the modifications varies greatly between the different materials. The average increases in the failure load test data are; 137% for the tungsten carbide, 86% for the nickel carbide, and 85% for the cast cobalt. The large variation between the tungsten carbide and the nickel carbide is, again, an unexpected result. These numbers compare with the average predicted increases in failure load of; 58.4% for the tungsten carbide, 60.5% for the nickel carbide, and 96.34% for the cast cobalt. It should be noted again that the cast cobalt valves do not include the undercut in the modified design so it is expected that the increase in failure load will be greater in these valves. The finite element models confirmed this prediction, however, this trend was not observed in the test data.

Again, it should be noted that the data presented here is useful only for comparison between the original and modified designs. The actual values are not useful in determining the load that the valves can handle in service because the effects of fatigue are not being considered.

4.2 Strain Gauge Study

Two very interesting failures were observed while testing the different valves. For both tests, the 222 410 N limit of the Instron was reached without the occurrence of a failure. When this limit was reached, the tests were stopped and the system unloaded. On both occasions the valves failed when the load had been reduced to around 111 000 N. The first failure was the 2" nickel carbide modified with undercut valve. This failure is indicated in Table 4.1 with two stars. The second failure occurred when repeating the test of a $2\frac{1}{4}$ " nickel carbide modified with undercut valve. These failures were investigated further.

4.2.1 Test Setup

To study these odd failures, a strain gauge was placed on a 2" modified with undercut nickel carbide seat, as shown previously in Figure 2.2. The gauge was positioned to measure the hoop strains on the outside surface, approximately half way up the lip. This position was chosen based on the finite element models which showed that the hoop strains in the lip region were the predominant strain in the valve. The valve was tested exactly as in the destructive tests, however, since this was not intended to be a destructive test, the load was only taken to 111 000 N and then removed. Strain and load data were collected using a chart recorder and a computer. The chart recorder was used to plot strain versus load. A very interesting and unexpected result was found.

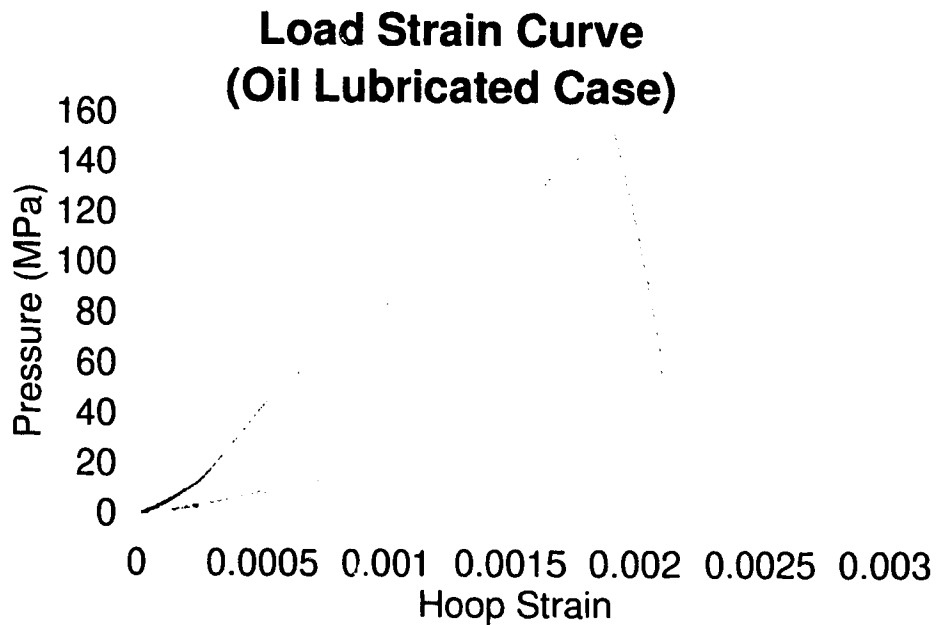


Figure 4.3: Load Strain Curve - Oil Lubrication

4.2.2 Test Results

The results of this test show that the point in the load curve where there is peak applied pressure is not necessarily the point where the strain is a maximum. In fact, when decreasing the applied load, the strain continues to increase on the order of another 10% until the pressure is only about $\frac{1}{3}$ of the peak value. The strain then decreases quickly and returns to zero strain for zero load. Figure 4.3 is a plot of this load strain curve. This figure shows a large hysteresis loop which includes an increase in hoop strain with a decrease in load. It was found that this curve is independent of the rate of loading and/or unloading.

To try to understand this reaction, two more similar tests were performed. Figure 4.4 shows the results of the first of these. The load was increased up to 122 500 N and then held constant for two minutes. This was done to test the stability of the system. No change in the strain was noted. The load was reduced to approximately

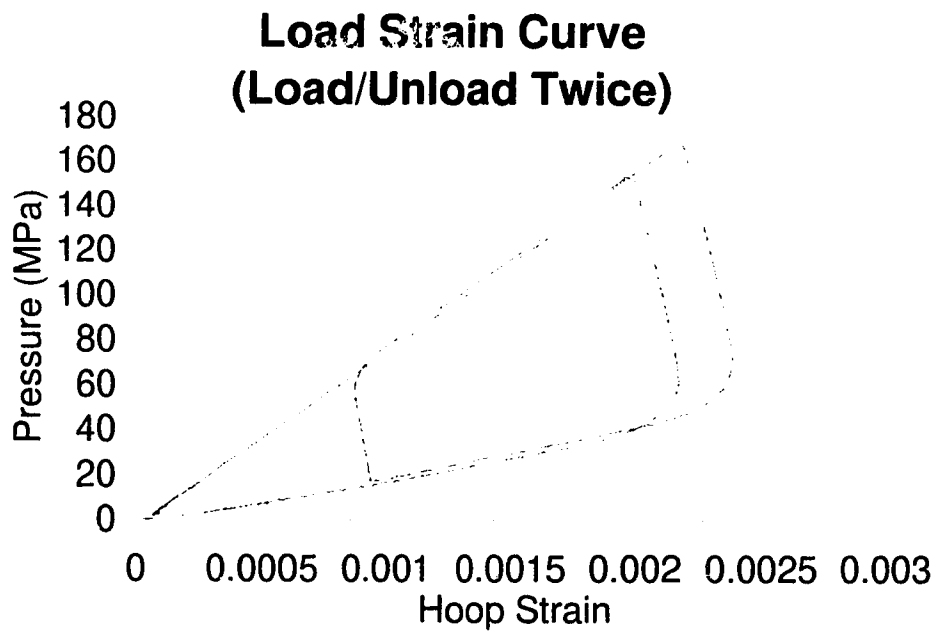


Figure 4.4: Reloading After Partial Unloading

11 100 N. The strain increased as it did in the first test and then decreased quickly, again at about $\frac{1}{3}$ of the peak load or 41 000 N. At 11 100 N, the load was held constant for about two minutes, again, to test the stability. The strain did not change. The load was then re-applied and held constant at 111 000 N. Initially, the strain decreased with the increasing load at the same rate that it had increased when the load was first decreased from 122 500 N (ie. The two curves have the same slope on the chart but in opposite directions). Where the reloading curve intersected the initial loading curve the strain began to increase again at a rate similar to the initial loading curve. Upon unloading fully, the strain again increased at a similar rate as in the last test and then decreased quickly below $\frac{1}{3}$ load (around 35 000 N) and returned to zero strain for zero load.

In the next test, the reaction to being unloaded to a point still higher than $\frac{1}{3}$ of the peak load (avoiding the change in slope at that point), and then reloaded was tested. These results are shown in Figure 4.5. In this test, the load was increased to 89 000 N and then decreased to 44 500 N and held constant. The strain increased with decreasing load at the same rate as before and then remained constant with the constant load. When the load was increased again, the strain decreased, following the unloading curve exactly. At 89 000 N the strain again began to increase along the initial loading curve. The load was increased to 111 000 N and then removed. The strain curve reacted exactly as before, returning to zero strain with zero load after showing an increase in strain followed by a sharp change in slope.

Since it is extremely unlikely that this would result from non-linear material properties, geometric and/or friction issues were considered. When the load is being increased, the ball is being pushed downward, wedging into the seat. The frictional force applied to the seat by the ball is in a downward and radially inward direction as shown in Figure 4.6. As the load is removed, the ball has a tendency to move upward, out of the seat. This results in a reversal in the direction of the frictional load on the surface of the seat as shown in Figure 4.7. The radial component of the frictional load changes from being directed inward while the load is increasing to being directed out-

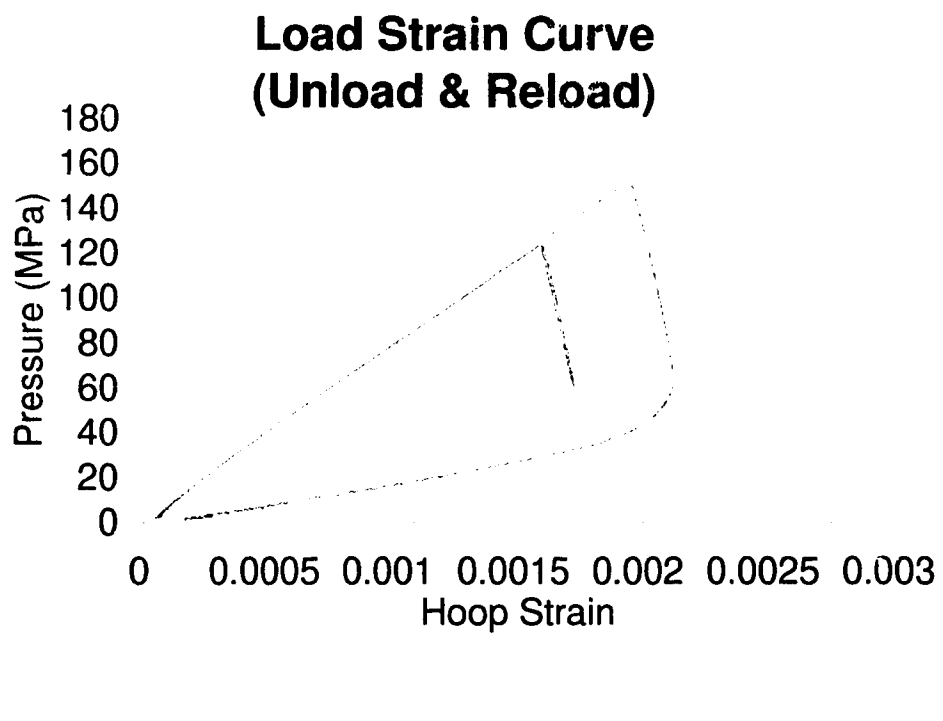


Figure 4.5: Unload to Before the Change in Slope and Reload

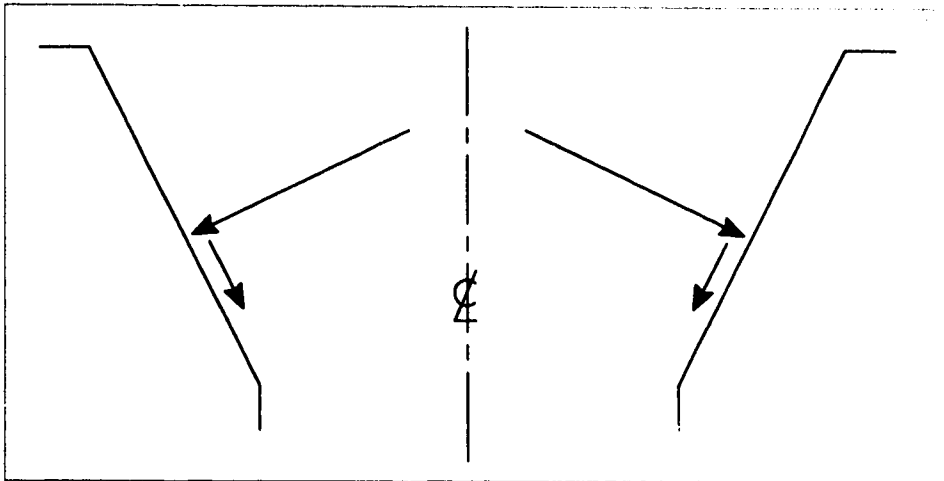


Figure 4.6: Normal and Frictional Load On Seat When Loading

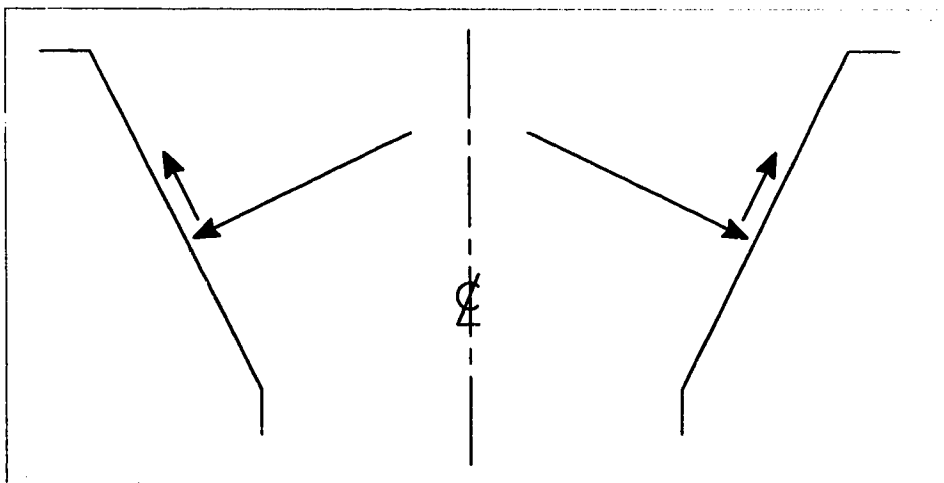


Figure 4.7: Normal and Frictional Load On Seat When Unloading

ward when the load is decreasing. This directional change is what causes the increase in strain with decreasing load. When the applied pressure begins to decrease, the rate of increase of the radial load due to friction is larger than the rate of decrease of the radial component of the normal load. The net radial load increases until the frictional sliding limit is reached and the ball begins to move out of the seat. At this point the normal load decreases substantially due to the reduced wedging of the ball into the seat. The strain begins to fall quickly, returning to zero strain with zero load. There are never any residual strains left due to the load cycle.

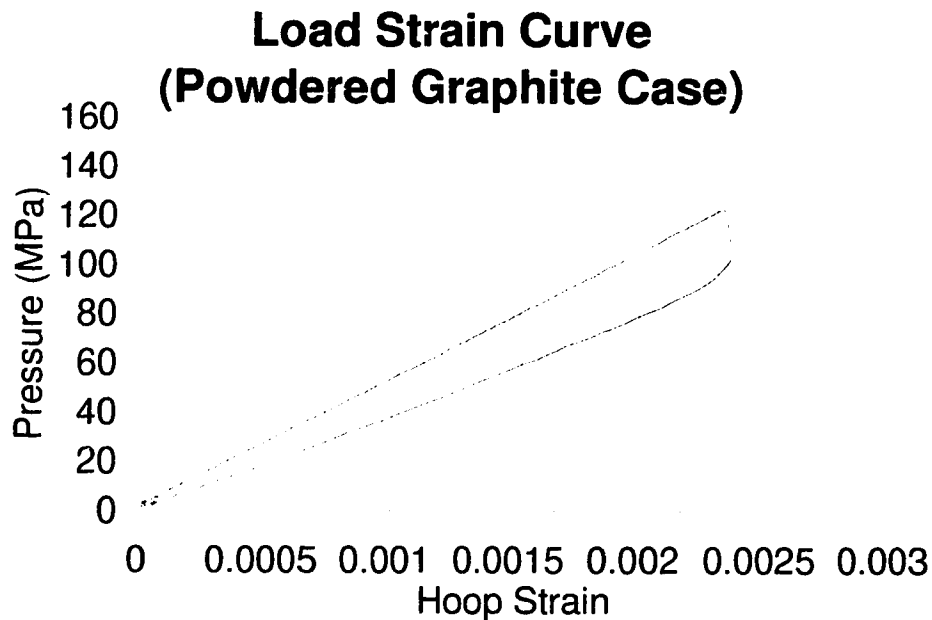


Figure 4.8: Load Strain Curve - Powdered Graphite Lubrication

A further test was done with reduced friction in an attempt to make a more realistic comparison to the frictionless finite element models and to test the validity of the previously described loading mechanism. To change the coefficient of friction between the two surfaces, powdered graphite was used instead of oil as a lubricant. The result of this test is shown in Figure 4.8. The area within the hysteresis loop has changed and the curves have different slopes compared with Figure 4.3. The hysteresis loop is much smaller and the strains for any given load are much higher than for the oil lubricated case. This lends weight to the earlier description of the loading mechanism on the seat. Upon loading, the net radial force is larger with the reduced friction, thus explaining the increased strains for any given load. Reduced friction also allows a reversal of motion to occur with less reduction in load, hence the smaller hysteresis loop.

The frictionless finite element model predicts no hysteresis loop while actual tests with 'nearly' frictionless conditions show a very small loop. Tests using oil as a

lubricant, as would be the case for valves actually in service, indicate a large hysteresis loop. Building models incorporating friction to compare against the oil lubricated tests, then, was the next logical step in this study.

Chapter 5

Frictional Contact Modeling

The results from testing indicate that friction plays a very large role in the distribution of strain, and therefore stress. Because of this, it was necessary to adapt finite element models to account for the frictional effects. The main objective of doing this was to attempt to correctly model the observed behavior.

No reference data is available regarding the frictional characteristics of the materials. This information must be inferred from a comparison of the load-strain data collected from the strain gauge study with the finite element models. Unfortunately, all the strain gauge tests were done using only cast cobalt balls. No data was collected to determine the frictional characteristics of tungsten carbide on tungsten carbide or nickel carbide on nickel carbide as would be the case in actual field applications. All models presented here, therefore, include a cast cobalt ball, regardless of which material the seat is made from.

5.1 Influence of Different Parameters

Before the frictional coefficients could be determined, it was necessary to understand how the other parameters in the analysis affect the results. These include modeling parameters such as the contact and sliding stiffnesses, symmetric versus asymmetric contact element meshing, and the location of strain measurement. Understanding how

changes in other parameters such as such as Young's Modulus and Poisson's Ratio can affect the results is also necessary.

5.1.1 Determining Contact Stiffness and Sliding Stiffness

Both the contact stiffness (KN) and the sliding stiffness (KT) are arbitrary parameters that must be set in the finite element models prior to generating the contact elements [11, 10]. These parameters are used to determine the reaction forces in the contact region on subsequent iterations.

The normal reaction force at a given node is determined by the equation:

$$F_{normal} = X_N * KN \quad (5.1)$$

where X_N is the depth that the node has penetrated the target surface. The value of KN should be chosen such that it is large enough to prevent over-penetration. A value of KN that is too small will allow the model to converge to a solution even though there is overlap of the two contacting surfaces. This will result in larger inaccuracies in the results. Setting the value too high will result in ill-conditioning of the system and it will not be able to converge to a solution. For accuracy, the best value to choose for KN is one which is slightly lower than the point where convergence is no longer possible. At this point, however, the model struggles to converge and, therefore, will use more iterations and, as such, more time to come to a final solution. As with choosing a mesh density, it is necessary to find a compromise between accuracy and the time needed to come to a solution. It is suggested that the value of KN be chosen using the equation:

$$KN = fEh \quad (5.2)$$

where f is "a factor that controls contact compatibility," E is Young's Modulus, and h is "a characteristic contact length." The normal range for the value of f is between 0.01 and 100. In this study, it was found that using a value of 2.4 for f caused ill-conditioning for most models. This value was 'backed off' by about 10% to 2.2 for all models. For cases where the contact is between two different materials (as it is in our

case, using only a cast cobalt ball and all three materials for the seat), the value used for E should be the larger of the two Young's Moduli. For axisymmetric problems it is suggested that the radius at the point of contact be used for the value of h .

The frictional reaction force is determined in much the same way as the normal reaction force. The software automatically defaults to using a value for KT which is 1% of KN . This value can, however, be specified explicitly. The program calculates a tangential reaction force at a given node using the equation:

$$F_{tangent} = X_T * KT \quad (5.3)$$

where X_T is the tangential distance that the node has moved since the last converged substep. (It is necessary to increase the load incrementally in substeps for non-linear analyses.) If this value is less than $F_N * \mu_{st}$, where μ_{st} is the static coefficient of friction, then the system is considered to be static and the force calculated in Equation 5.3 is used as the frictional reaction force. If the value is higher than $F_N * \mu_{st}$ then the system is considered to be kinetic and the frictional reaction force is calculated using:

$$F_{tangent} = F_{normal} * \mu_k \quad (5.4)$$

where μ_k is the kinetic coefficient of friction.

When the system is considered to be static, Equation 5.3 is used as the reaction force to move the node back to its location from the last converged substep. Lower values of KN will result in lower reaction loads and as such there may be a small amount of slipping of the nodes across the contacting surface even though the system is considered to be static. This introduces inaccuracies to the results (sliding in a static case) and is analogous to the problem of over-penetration for a low value of KN . Setting the value of KT too high will result, again, in an ill-conditioned system. The optimum point for accuracy will be that which is slightly lower than that where convergence no longer occurs. For this study, it was found that setting the value of KT to be 5% of the value for KN works well.

5.1.2 Sensitivity to Small Changes in Young's Modulus and Poisson's Ratio

The manufacturers of the valves could provide no indication of how accurate the values provided for Young's Modulus were for the different materials. Values for Poisson's Ratio could not be provided at all. Because of this, it was necessary to perform sensitivity analyses to determine how significant changes in Young's Modulus and Poisson's Ratio are to the final results.

Values were provided by the manufacturers of the valves for Young's Modulus for all the materials. Since it is not possible to determine the accuracy of these values without performing testing, it is necessary to use the provided values with an understanding of how changes in Young's Modulus affect the final results. Table 5.1 summarizes the data collected from three models using different Young's Moduli. The

Table 5.1: Effect of Young's Modulus on Results

| Test Case | A | B | C |
|-------------------------|-----------|-----------|-----------|
| Young's Modulus | | | |
| Cast Cobalt Ball | 136530MPa | 151700MPa | 166870MPa |
| Nickel Carbide Seat | 527490MPa | 586100MPa | 644710MPa |
| Peak Coulomb-Mohr Ratio | 0.8377 | 0.8399 | 0.8396 |
| Hoop Strain | 0.001606 | 0.001765 | 0.001952 |

load used is that used for the strain gauge study. This load was chosen so that direct comparisons could be made to the load strain curves from the strain gauge study. In test case 'B' the values of the Young's Moduli for the ball and the seat were the values supplied by the manufacturers. In test cases 'A' and 'C', the values of the Young's Moduli were either increased or decreased by 10% from the values in test case 'B'. These results show that the peak Coulomb-Mohr Ratio is affected very little by the changes in Young's Modulus. The value of the hoop strain at the location where the strain gauge is located on the test specimen changes by 10% with the changes in Young's Modulus. The implications of this are that the data obtained for the failure predictions is relatively insensitive to changes in Young's Modulus and as such the accuracy of the Young's Modulus data is not critical. The relatively large difference

in the hoop strain data may have an affect on how accurately the coefficient of friction can be determined as described in Section 5.2.

An initial value of 0.3 was chosen for Poisson's Ratio. This choice was based solely on the fact that it is a common value for most metal compounds. Without the aid of material testing, there is no way to verify the accuracy of this assumption. Instead, a sensitivity analysis was done to determine how the results are affected by changes in Poisson's Ratio. Models of a 2" nickel carbide original design valve were built using values for Poisson's Ratio ranging from 0.2 through 0.4. Table 5.2 summarizes these results. The numbers presented are the peak Coulomb-Mohr ratio and the hoop strain

Table 5.2: Effect of Poisson's Ratio on Results

| Poisson's Ratio | 0.2 | 0.25 | 0.3 | 0.35 | 0.4 |
|-------------------------|----------|----------|----------|----------|----------|
| Peak Coulomb-Mohr Ratio | 0.7713 | 0.7879 | 0.8399 | 0.8928 | 0.9460 |
| Hoop Strain | 0.001713 | 0.001742 | 0.001765 | 0.001790 | 0.001812 |

at the location where the strain gauge was mounted for the strain gauge study. It is evident that these large changes in Poisson's Ratio introduce about a 10% variation to the Coulomb-Mohr ratio and less than a 3% variation to the hoop strain data. It is likely that the true value for Poisson's Ratio is fairly close to 0.3, so choosing this value, then, will affect the accuracy of the final solution little.

5.1.3 Symmetric Meshing

For all the models in this study, point to surface contact elements were used [10, 11]. For these elements, one surface is considered to be the contacting surface and the other to be the target surface as shown in Figure 5.1. The 'point' is simply a single node (K) on the 'contacting surface.' The 'surface' is a line joining two adjacent nodes (I,J) on the 'target surface.' When the point crosses the line defining the surface and the point is within a radius of 1.5 element widths from the center of that line, as in Figure 5.2, then contact is considered to have occurred and reaction loads are calculated to keep the point 'near' the surface. If the contact node is outside the circle then the contact

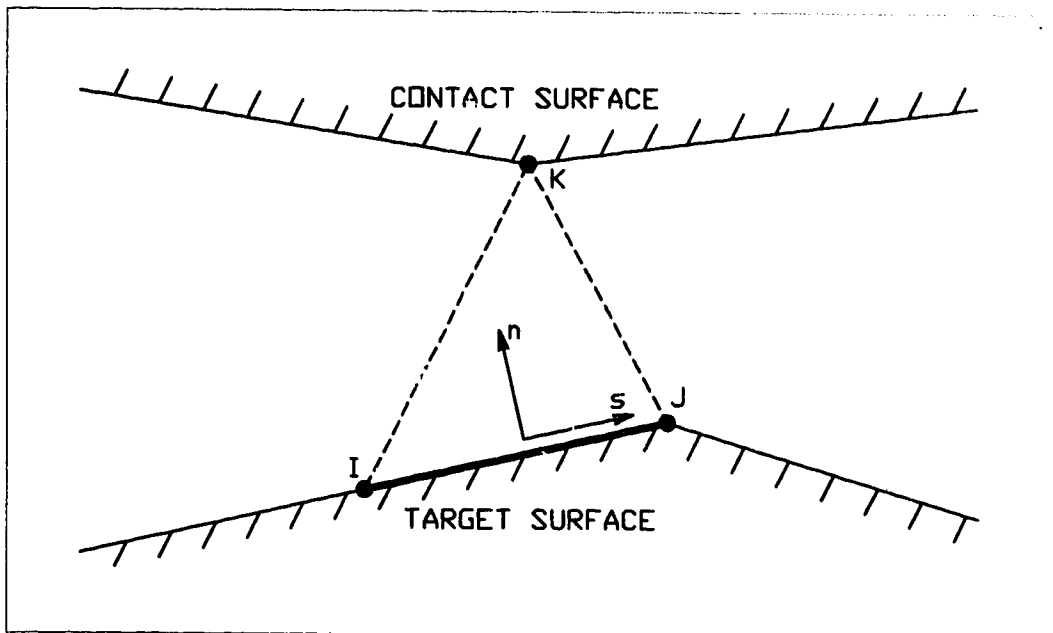


Figure 5.1: Drawing of a Point to Surface Contact Element

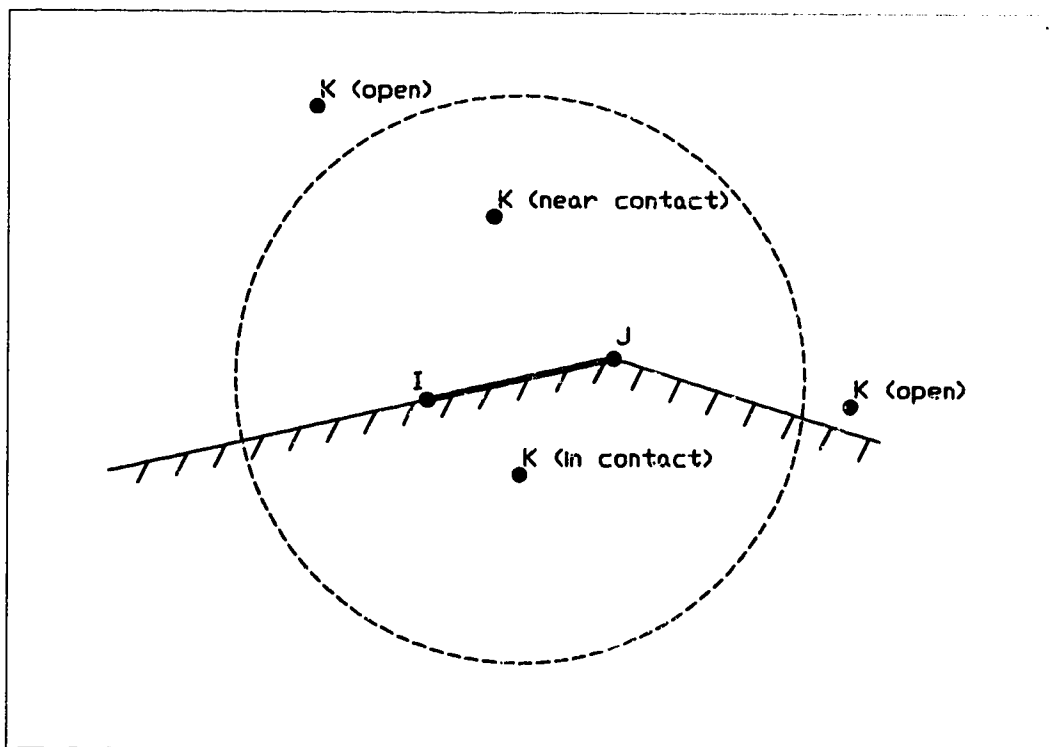


Figure 5.2: Drawing Showing When a Contact Element is Considered

element is not considered active (even when the node has crossed the line defining the target surface). Often, when too large a substep is taken when incrementing the load, a contact node is pushed through the surface and out the far side of the circle. The element is no longer considered active and no reaction loads are generated. The two surfaces cross over each other and the analysis fails. This is why it is necessary to apply small substeps to increment the load when using contact elements.

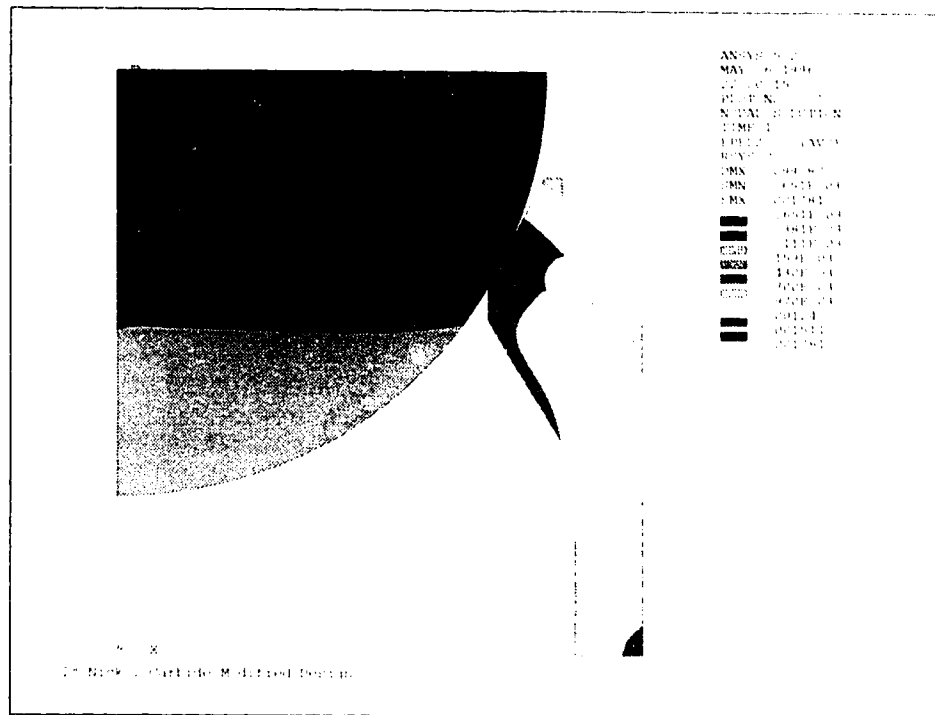
When the elements are generated once, with one surface as the target surface and the other as the contacting surface, it is called asymmetric meshing. Meshing the elements a second time with the target and contacting surfaces reversed results in two sets of contact elements overlapping each other between the two surfaces. This is symmetric meshing of the contact elements. Symmetric meshing is the recommended approach of the developers of the finite element software.

Meshing the contact elements in this way greatly increases the numerical stability of the model as compared to asymmetric meshing. Even though there are more elements to consider when solving a model using symmetric meshing, the convergence times are shorter because fewer iterations are necessary. The increased stability also means that the contact and sliding stiffnesses can be increased to improve accuracy without increasing the convergence times.

5.1.4 Location of Strain Measurement

It is also important to determine if the location at which the strain was measured has a significant effect on the results. It is also necessary to determine the strain gradient along the surface where the measurements were taken. If the strain gradient is non-linear then it is necessary to take an integrated average of the strain data from the model over the width of the actual strain gauge to compare with the test data. If the gradient is small or nearly linear then simply using the value at the location of the center of the strain gauge will suffice.

The strain gauge study was done with a 2", modified with undercut, nickel carbide valve. The contour plot representing hoop strain in this valve is shown in Figure 5.3.



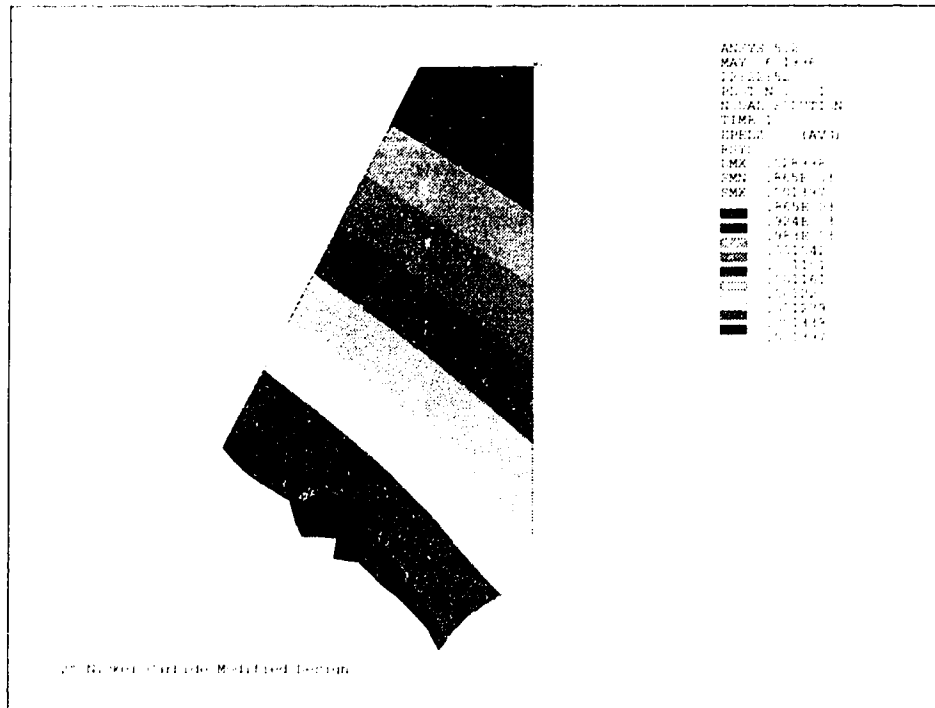


Figure 5.4: Hoop Strain Distribution - Breakaway of Lip Region

5.2 Determining the Frictional Coefficients

As seen earlier in the strain gauge study in Section 4.2.2, the coefficient of friction plays a major role in how the valve behaves. With lower friction as with the powdered graphite lubrication, the strains are much higher for any given load than for the oil lubricated case. Since the normal operation of the valve is in an oil environment it is necessary to determine the coefficient of friction for the different materials with oil as a lubricant. Determining the correct value for the coefficient of friction was basically a trial and error process of comparing the load strain curves from the strain gauge study to the curves generated in the finite element models. In the models, the static and dynamic coefficients were made equal. This value was changed from model to model until the curves matched reasonably well. Figure 5.5 shows how the hoop strain results change when using different coefficients of friction for a 2" nickel carbide seat with a cast cobalt ball. The coefficient of friction was varied from 0 (ie. frictionless) up to a value of 0.20. As expected, the hysteresis loop became larger and the strain

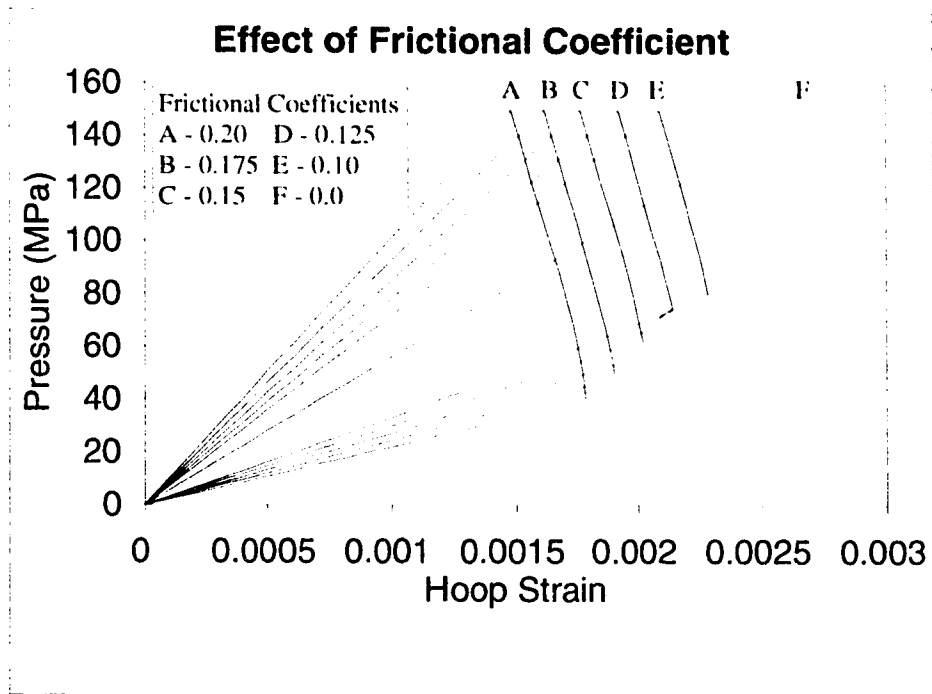


Figure 5.5: Reaction to Changing the Coefficient of Friction

at any given load decreased with increased friction. It was found that a coefficient of 0.145 matched the curve found in Figure 4.3 well. Figure 5.6 shows the curve from Figure 4.3 overlaid with the curve obtained using a coefficient of friction of 0.145. The predicted curve is similar to the actual data but not exact. Although the curves are very close when the valve is being loaded up, the loop observed when unloading is somewhat smaller in the predicted case. Varying Young's Modulus as in Case 'C' from Table 5.1 will increase the strain values. Increasing the coefficient of friction will then decrease the strain to the proper level and also increase the size of the loop. The curves would then match more closely. This, however, involves modifying more than one parameter with little evidence to support that it is the correct course of action. The predicted curve, as it is shown in Figure 5.6, is reasonably close to the observed results. Since we are mainly interested in the relative increase in strength of the valves, the models are adequate without making changes to the value of Young's Modulus. The value for the coefficient of friction for tungsten carbide seat with a cast

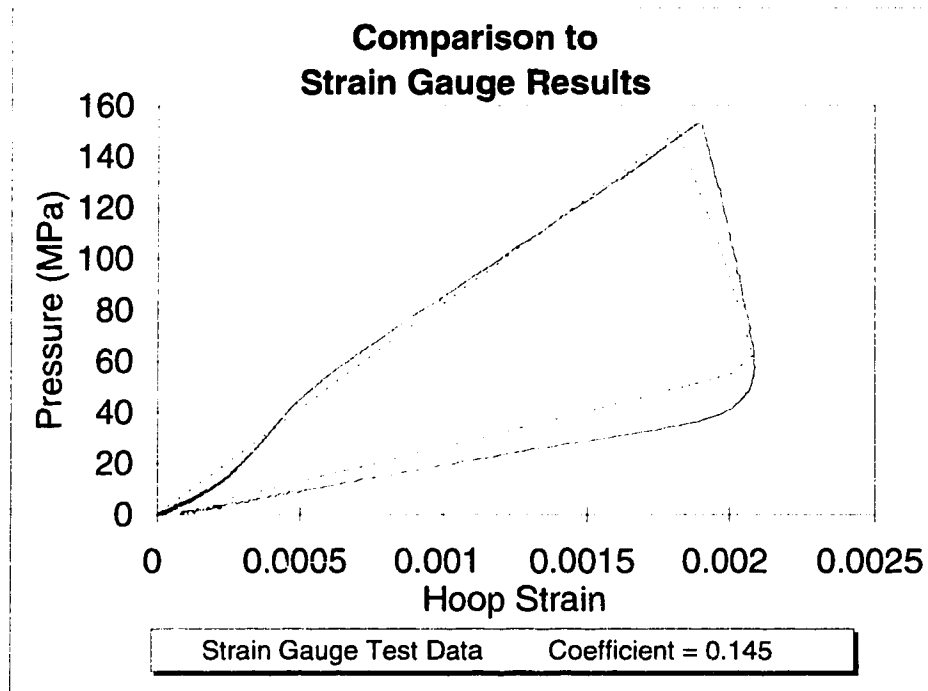


Figure 5.6: Comparing Test Data to Curve Using a Frictional Coefficient of 0.145 cobalt ball which resulted in curves which closely matched the test data was 0.15. For the cast cobalt ball on a cast cobalt seat this value was found to be 0.17.

5.3 Failure Predictions

After reasonable values for the coefficients of friction between the cast cobalt ball and the three materials for the seats were determined, it was possible to do further failure predictions. Models were generated for each valve size in each material. The load was incremented for each model until the peak Coulomb-Mohr ratio was 1.00 ± 0.01 . A summary of these loads is presented in Table 5.3 beside the frictionless predictions presented earlier in Table 4.1. In all cases, the failure load predicted by the model including friction is approximately twice that predicted by the frictionless model. It was noted in the data collected from the strain gauge study presented in Section 4.2.2 that the strain was much higher for a given load in the case with graphite lubrication

Table 5.3: Frictional Versus Frictionless Failure Load Predictions

| Size | Frictionless Original Design (N) | Frictional Original Design (N) | Frictionless Modified w/ Undercut (N) | Frictional Modified w/ Undercut (N) |
|---|---|---|--|--|
| Tungsten Carbide | | | | |
| 1 $\frac{1}{4}$ " | 32170 | 61230 | 57075 | 107915 |
| 1 $\frac{1}{2}$ " | 68230 | 128440 | 116395 | 263290 |
| 1 $\frac{3}{4}$ " | 162260 | 287510 | 204960 | 417330 |
| 2" | 124040 | 232040 | 210140 | 423205 |
| 2 $\frac{1}{4}$ " | 296900 | 523335 | 439410 | 878815 |
| Nickel Carbide | | | | |
| 1 $\frac{1}{4}$ " | 20755 | 40480 | 37150 | 71615 |
| 1 $\frac{1}{2}$ " | 45355 | 84295 | 116395 | 183825 |
| 1 $\frac{3}{4}$ " | 105325 | 204950 | 133795 | 279550 |
| 2" | 78805 | 145925 | 111640 | 280925 |
| 2 $\frac{1}{4}$ " | 188430 | 383190 | 281065 | 530450 |
| Cast Cobalt (Undercut Not Included In Modification) | | | | |
| 1 $\frac{1}{4}$ " | 9340 | 16280 | 21375 | 43595 |
| 1 $\frac{1}{2}$ " | 18060 | 35120 | 47560 | 73040 |
| 1 $\frac{3}{4}$ " | 41560 | 89385 | 60635 | 105335 |
| 2" | 32105 | 59830 | 65670 | 121860 |
| 2 $\frac{1}{4}$ " | 76800 | 219320 | 102925 | 245435 |

than for the oil lubricated case. This again supports the trend in the predictions seen in Table 5.3. Failure is expected to occur at lower loads for cases with lowered friction.

There is a noticeable trend that can be seen when comparing the frictional predictions with the actual test data presented in Table 4.1. For the $1\frac{1}{4}$ " valve size, the frictional predictions are close to the actual test data. For all other sizes, however, the predicted failure load is higher than the tested failure load by as much as a factor of 2.5. This factor seems to increase as the valve size is increased.

One possible explanation of the difference between the predicted and actual failure loads is that the Coulomb-Mohr failure criterion does not take into account all the aspects of the failure mechanics. This criterion assumes that the surface is completely free of defects. In fact, there are many flaws in the surface of the valves. According to work done by A. A. Griffith in the early 1920's [9, 4], glass was observed to have a strong relationship between strength and the size of the sample. Larger samples tended to break at lower stress levels than did smaller samples. This is attributed to the larger sample having more (and potentially larger) defects than the smaller sample. This was also shown to be true for ceramics and other brittle materials. This could be an explanation of what appears to be a decrease in the strength of the larger valves compared with the smaller valves. Again, this discussion comes back to having insufficient information regarding the material properties. To properly investigate this possibility it is necessary to know what the fracture toughness of the various materials is. It is also necessary to know the relative size of the flaws or microfractures. Neither of these pieces of information is available without extensive testing which is beyond the scope of this work.

Assuming that this explanation is correct it is possible to say that the Coulomb-Mohr failure criterion is not adequate for predicting the failure load for each valve. This criterion does correctly predict the location of initiation of failure and does adequately show the relative increases in strength associated with the various modifications. For this study, the actual load at failure is not as important as the relative change in the failure load due to the modifications. For this reason, the Coulomb-Mohr

failure criterion is adequate and further investigation into the actual mechanisms of the fracture mechanics was deemed unnecessary.

Chapter 6

Conclusions and Future Work

The goals of this study were to determine the failure mechanisms of the guided stem design and, based on this, make changes to this design to improve the structural performance. Over the course of this study, the failure mechanism was determined and modifications to the design were implemented which had a positive effect on the performance of the valves. As such, the goals of the study were achieved.

A large majority of the failures observed in valves operating in the field consisted of portions of the upper lip being broken off. Most of these failures featured vertical fracture surfaces near the top edge of the lip and horizontal fracture surfaces where the lip met with the shoulder. The vertical fracture surface indicated that a possible failure mode was one which resulted from tensile hoop stresses. Finite element modeling of the valves verified that this was, in fact, the dominant stress condition and was the likely cause of the failures. The tensile hoop stresses observed were the result of a relatively large outward deflection of the upper ring due to the wedging action of the ball. To improve the structural performance of the valves, it was necessary, then, to reduce the radial deflections.

Two changes were made to the design for the purpose of reducing the radial deflection of the upper ring. The first modification involves grinding back the contacting surface of the seat so that the point of contact is lowered. This reduces the stresses for two reasons. Firstly, the point of contact is closer to the thicker part of the material

resulting in a larger distribution of the stresses throughout the body and also less deflection. Secondly, the lowered contact point reduces the effective moment arm of the radial component of the reaction force, thus reducing the amount of bending that the force can cause. The second modification involves altering the angle of incidence between the ball and the seat to reduce the radial component of the reaction force. The axial component of the reaction force is constant for any given pressure. The normal force and, hence, the radial component are affected by the contact angle. By increasing the contact angle (from vertical), the normal force and, more importantly, the radial component of this force are reduced. This reduced radial load results in less deflection of the upper ring and, therefore, reduced hoop stress levels.

Destructive tests were done in an attempt to verify the finite element model and to prove that the changes proposed were effective. It was found that the predicted and actual failure loads were not closely related for most valves. This discrepancy is likely the result of the failure criterion used in the analysis of finite element models. The Coulomb-Mohr failure criterion does not take into account parameters such as surface finish and fracture toughness which are important considerations for brittle materials. This is an area in which further research could be done, however, the gains may not be appreciable from the point of view industry (the relative increase in strength is the important aspect for industry). Although the actual values were dissimilar, the relative differences between the original design and the modified design matched fairly well between the test data and the finite element models. This relative difference between the failure loads is more important in this study than the actual failure loads themselves as the values are only representative of a static load case. The effects of fatigue were not considered in this study. In the field, the valves are subjected to cyclic loading and actually fail at much lower loads than those observed in the lab and predicted with the finite element models. Fatigue is an important aspect of the failures modes observed in valves in service. A proper fatigue analysis complete with testing is another area which could warrant further consideration.

The design changes that were available for this study were limited to being a retrofit

of the existing design. A study that would be of great interest would be the complete redesign of the valve without the restriction of retrofitting the existing design. In the API (unguided) design, a sphere is the necessary shape for the ball as it is free to rotate about all three axes but still must make contact with a circle. The guided stem design, however, is only free to rotate about one axis. This means that the only restriction on the shape of the ball is that it must be axisymmetric to maintain the circular contact. The hemisphere does fall into this category, however, it is not the most efficient shape structurally nor with respect to the hydrodynamic efficiency of the valve. A more appropriate shape to improve the structural performance would have horizontal surfaces where the ball and the seat make contact. This would eliminate the radial component of the reaction force completely and leave the structure almost entirely in compression. The materials used are far better in compression than in tension and as such the strength of the valve would be many times larger than currently possible with the hemispherical design for the ball. It is possible that the horizontal surfaces would cause large disturbances in the flow and reduce the hydrodynamic efficiency of the valve and possibly increase wear of the components. It is also possible that not enough pressure would be applied between the ball and the seat to form an effective seal without the wedging action of the angled contact surface. Other shapes could be experimented with to find an optimum balance between the hydrodynamic and structural performance of the valves. Completion of a study of this nature would be a very large step forward for this technology.

Bibliography

- [1] Eugene A. Avallone and Theodore Baumeister III, editors. *Mark's Standard Handbook for Mechanical Engineers*. McGraw Hill, New York, 9th edition, 1987.
- [2] Arthur P. Boresi and Omar M. Sidebottom. *Advanced Mechanics of Materials*. John Wiley & Sons, New York, 4th edition, 1985.
- [3] David Broek. *Elementary Engineering Fracture Mechanics*. Martinus Nijhoff, The Hague, The Netherlands, 3rd revised edition, 1982.
- [4] Richard A. Flinn and Paul K. Trojan. *Engineering Materials and Their Applications*. Houghton Mifflin, Boston, MA, 3rd edition, 1986.
- [5] American Petroleum Institute. *Recommended Practice for Care and Use of Subsurface Pumps; API Recommended Practice RP111AR*. American Petroleum Institute, Washington, DC, 3rd edition, June 1989.
- [6] Petrovalve International. Petrovalve plus [video], 1994. Houston, TX.
- [7] Petrovalve International. Petrovalve plus [brochure], 1996. Edmonton, AB.
- [8] Kenneth S. Edwards Jr. and Robert B. McKee. *Fundamentals of Mechanical Component Design*. McGraw Hill, New York, 1991.
- [9] N. H. Polakowski and E. J. Ripling. *Strength and Structure of Engineering Materials*. Prentice-Hall, Englewood Cliffs, NJ, 1966.
- [10] Swanson Analysis Systems, Inc., Houston, PA. *ANSYS User's Manual for Revision 5.0; Volume I, Procedures*, 1994.

- [11] Swanson Analysis Systems, Inc., Houston, PA. *ANSYS User's Manual for Revision 5.0; Volume IV, Theory*, 1994.